Structure and Instability of the Ekman Spiral in the Presence of Surface Gravity Waves*

ANAND GNANADESIKAN AND ROBERT A. WELLER

Department of Physical Oceanography, Clark Laboratory, Woods Hole Oceanographic Institution, Woods Hole, Massachusetts

ABSTRACT

The physical processes responsible for maintaining the mixed layer are examined by considering the velocity structure. The low-frequency Ekman response in the interior of unstratified mixed layers is much less sheared than is predicted using eddy viscosity models that reproduce the temperature structure. However, the response is more sheared than predicted by models that parameterize the mixed layer as a slab. An explanation is sought by considering the effect of an infinite train of surface gravity waves on the mean Ekman spiral. For some realistic conditions, the Ekman spiral predicted by assuming small-scale diffusion alone is strongly unstable to Langmuir cells driven by wave-current interaction. In the Northern Hemisphere, these cells are oriented to the right of the wind, the result of a balance between maximizing the wave-current forcing, maximizing the efficiency of this forcing in producing cells, and minimizing the crosscell shear. The cells are capable of replacing small-scale turbulent diffusion as the principal transport mechanism within the mixed layer. Finite-difference code runs that include infinite-length trains of surface gravity waves qualitatively explain the reduction in shear within the mixed layer relative to that predicted by small-scale mixing. However, the theory also predicts an Eulerian return flow balancing the Stokes drift that has not been observed.

1. Introduction

There exists at present a lack of understanding of how the oceanic mixed layer is maintained. This uncertainty is reflected in attempts to model the velocity structure. Although the upper layer of oceans and lakes is often very well mixed with respect to scalar quantities such as temperature, salinity, and density, significant velocity gradients may be found within it. A number of investigators (Richman et al. 1987; Weller and Price 1988; Gnanadesikan 1994; Weller and Plueddemann 1994) report the existence of strong shears within the isothermal mixed layer, varying on superinertial frequencies (1–30 cph) as well as on longer timescales coherent with the surface stress. Despite this fact, many models of the mixed layer treat it as a slab within which velocity as well as all scalar quantities are instantaneously and completely mixed (Denman 1973; Davis et al. 1981; Price et al. 1986, henceforth PWP). The response of the near-surface velocity to wind forcing in these slab models is thus sheared only below the minimum mixed layer depth. This paper uses a PWP mixed

layer model [described in section a(1) of the appendix] as a baseline slab model.

Classically, attempts to model the shear within the mixed layer have followed the approach of Ekman (1905) in which the local momentum transport is parameterized by an eddy viscosity ν_e multiplied by the local shear $\partial v / \partial z$. The divergence of this momentum transport then balances the time rate of change of the velocity and the Coriolis force $2\Omega_p \times v$:

$$\frac{\partial v}{\partial t} + 2\Omega_p \times v = \frac{\partial}{\partial z} \nu_e \frac{\partial v}{\partial z}, \tag{1}$$

where Ω_p is the planetary vorticity and the bold letters denote vectors. The problem of how to parameterize the eddy viscosity has, however, proven to be extremely difficult. Huang (1979) presented over 80 different published values and parameterizations, which showed no systematic agreement. The most self-consistent of these parameterizations are probably the turbulence closure schemes of Mellor and Yamada (1974) in which turbulence is produced by local shear and buoyancy instability. This paper uses a Mellor–Yamada level 2 (MY2) turbulence closure model in which gradients of velocity and density at a given point produce turbulence that is balanced by dissipation (see appendix section a(2) for a more complete description).

Tests of different mixed layer models have traditionally focused on how well the models predict the density or temperature structure of the mixed layer. In this respect, both models do quite well. Figure 1 shows data from the Mixed Layer Dynamics Experiment (hence-

Corresponding author address: Dr. Anand Gnanadesikan, Program in Atmospheric and Oceanic Sciences, Sayre Hall, Princeton University, P.O. Box CN710, Princeton, NJ 08544-0710.
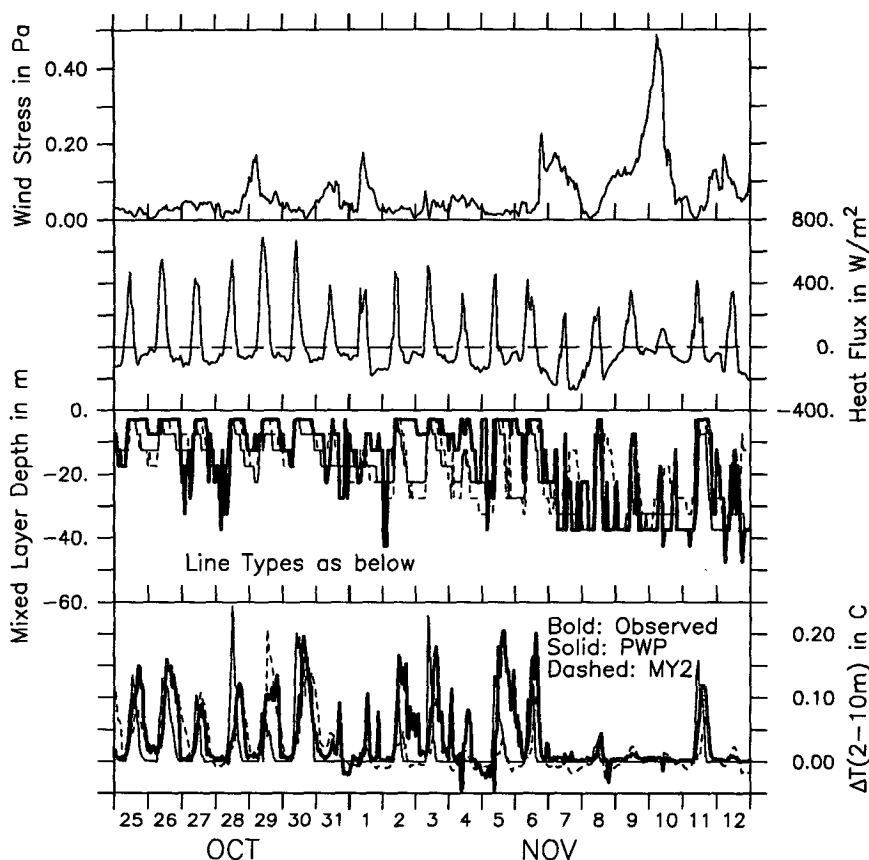E-mail: alg@gfdl.gov

FIG. 1. Surface forcing and temperature structure during MILDEX. (a) Wind stress in pascals calculated using bulk fluxes. (b) Heat flux in watts per square meter. (c) Mixed layer depth defined as the minimum depth at which the temperature was 0.02°C different from the surface. Bold lines are observed, solid lines predicted from the PWP model, and dashed lines predicted from a Mellor–Yamada level-2 turbulence closure model. (d) Temperature difference between 2- and 10-m depth. Line convention is the same as in (c).

forth MILDEX) that demonstrates this fact. The data shown were collected from the Research Platform *FLIP* using vector measuring current meters (VMCMs). Details of the data collection are given in Weller and Price (1988) and Gnanadesikan (1994). The PWP model and Mellor–Yamada level-2 model were both forced with the wind stress and heat flux shown in Figs. 1a and 1b. The models reproduce the mixed layer depth (Fig. 1c) and the temperature stratification between 2 and 10 m (Fig. 1d). In general, the two models agree closely with the data, showing a mixed layer that becomes shallow during the day and deepens at night. The major differences occur between 2 and 4 November, a time when the winds are weak and there is a good deal more stratification in the upper 10 m than predicted by the model. Analysis of the heat budget indicates that much of this stratification is due to frontal activity. As the winds strengthen later on in the experiment, the mixed layer is deeper and the upper 10 m do not become strongly stratified in both the models and the data.

The mean velocity profiles predicted by the two models, however, are systematically different from each other and from the data. Figure 2 shows the low-frequency Ekman response over five inertial periods beginning at 0200 UTC (local time lags by 8 hours) 6 November. During this interval the winds were strong and the mixed layer did not restratify. The low-frequency responses in the data and the models [calculated by rotating the velocity into a wind-relative coordinate system and averaging, a method documented more extensively in Weller et al. (1991); Gnanadesikan (1994); Schudlich and Price (1994)] are quite different. The data show a velocity response that is strongest in the middle of the mixed layer. Over depths of 5–20 m this response is extremely uniform. The PWP model predicts a response that is essentially slablike down to a depth of 35 m, underestimating the shear at both top and bottom of the mixed layer. The MY2 model predicts a response that looks very much like a classical Ekman spiral. The response is sheared throughout the
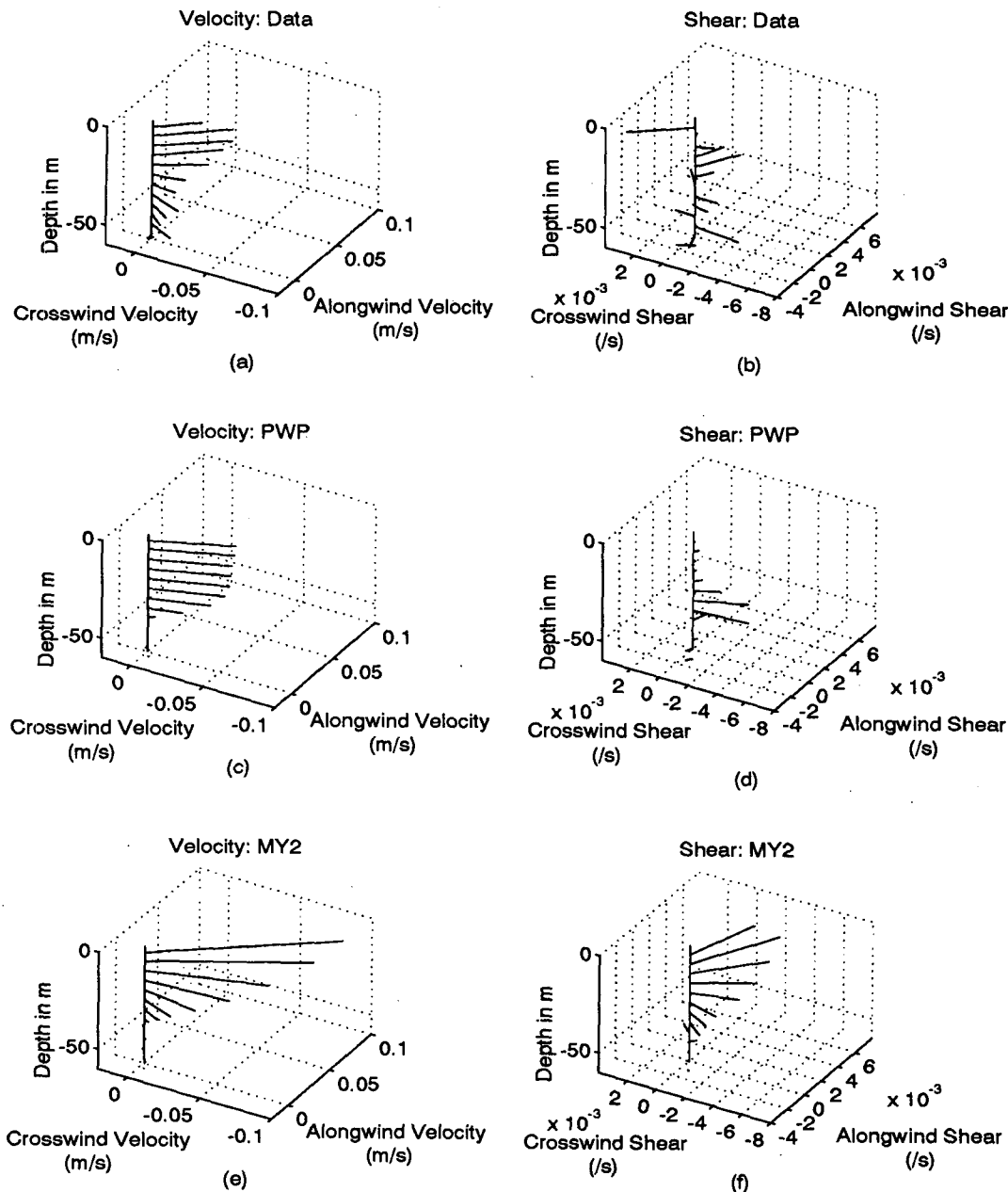
FIG. 2. Subinertial velocity and shear relative to the wind during MILDEX. Calculated by orienting velocities relative to the wind and averaging over time. For the velocity response, the velocity at a depth of 60 m was subtracted to eliminate the geostrophic flow. Responses are shown for 6–11 November 1983, when Langmuir cells were strong. (a) Velocity with respect to 60 m, relative to wind data. (b) Shear relative to wind from data. (c) Predicted velocity relative to wind, PWP model (slab mixed layer). (d) Predicted shear relative to wind, PWP model. (e) Predicted velocity relative to wind, MY2 model. (f) Predicted shear relative to wind, MY2 model.

mixed layer, greatly overestimating the shear in the middle of the mixed layer. These differences reflect uncertainties in the physics of present parameterizations of mixing within the mixed layer.

This paper suggests that the models may fail to reproduce the shear structure because they do not properly include the effects of large eddies (Langmuir circulations) within the mixed layer. While such large eddies are capable of homogenizing the mixed layer relative to the highly sheared profile predicted by the MY2 model, they do not mix it completely and instantaneously as predicted by slab models. As a result, the velocity profile in the presence of such large eddies differs significantly from that predicted by both of the

models. This paper considers large eddies, which are primarily driven by wave–current interaction rather than by the shear instability process known to be important in the atmospheric boundary layer (Brown 1970) or by buoyant overturning. This wave–current interaction mechanism is absent from both the PWP and MY2 models and thus provides an extra source of mixing. When fully developed Langmuir cells are included in a model of the mixed layer, the resulting shear profile is less sheared than predicted by the MY2 model but more sheared than predicted by the PWP model.

The paper proceeds as follows. Section 2 introduces the equations of motion for a mixed layer with two-dimensional Langmuir cells in the presence of Coriolis forces. Section 3 solves for the low-frequency, one-dimensional, response of this idealized layer to an infinite train of surface gravity waves, thus defining the initial condition on which the cells grow. Section 4 demonstrates that a wide range of Ekman spirals are unstable to Langmuir cells. Section 5 considers the physical processes that drive the cells and argues that wave–current interaction is the most important mechanism. Section 6 shows that the Ekman spiral predicted by the MY2 model during MILDEX is unstable to Langmuir cells driven by wave–current interaction. Section 7 demonstrates that, when the unstable cells grow to finite amplitude, they are capable of substantially modifying the velocity structure of the mixed layer. Section 8 concludes this paper.

2. The equations of motion

A schematic of the way in which we include Langmuir circulation in the mixed layer is shown in Fig. 3. Langmuir circulation consists of an array of vortices (Langmuir 1938), oriented at some angle α to the wind. In the Northern Hemisphere, α tends to be positive so that the vortices lie to the right of the wind (Faller 1964), a phenomenon which will be discussed in more detail in section 5. For purposes of this paper, the alongcell direction is the y direction. The velocity in this direction is denoted by v and the vorticity in this direction is denoted by Ω. The crosscell horizontal direction is the x direction and the velocity in this direction is denoted by u. The vertical direction is the z direction (increasing upward), and the velocity in this direction is denoted by w. The vortices tend to be asymmetric, with stronger downwelling W_{down} than upwelling (W_{up}) velocities. Estimates of W_{down} range from 0.01 to 0.25 m s^{-1} (Leibovich 1983). Surface convergence zones are associated with jets of water that move more quickly in the alongcell direction than the remainder of the mixed layer. The amplitude of the jet V_{jet} is of order 0.05 m s^{-1}.

The most widely accepted theory for the generation of Langmuir cells, that of Craik and Leibovich (1976), assumes that the cells are driven by interactions between surface gravity waves and the Eulerian current
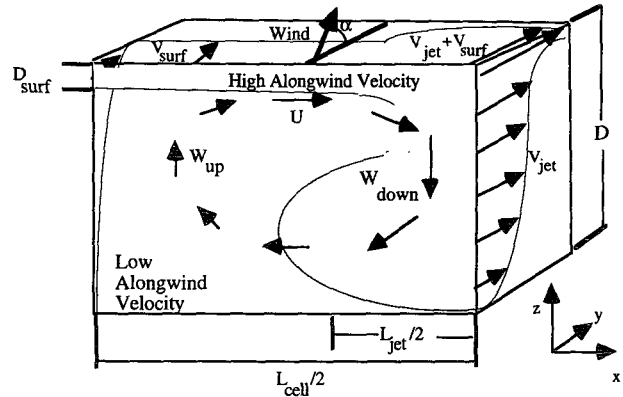

FIG. 3. A schematic of Langmuir circulation illustrating the concepts found in the text. Helical vortices with horizontal velocities U, upwelling velocity W_{up}, and downwelling velocity W_{down} are oriented at some angle α to the wind. Within the downwelling zones water moving quickly in the alongwind direction (shown by the stippling) is advected downward.

field. Thus, in order to model Langmuir cells within an Ekman layer it is necessary to derive equations that include surface gravity waves, capturing their effect both on the mean current and the cells. Suppose the equations of motion are as follows:

$$\frac{\partial u}{\partial t} + \nabla \frac{1}{2} u^2 + (\omega + f\mathbf{k}) \times u = -\frac{\nabla p}{\rho} + \nu_e \nabla^2 u,$$

$$(2)$$

where ω is the relative vorticity, $f\mathbf{k}$ is the vertical component of the planetary vorticity, and the bold letters denote vector quantities.[1] Suppose that an averaging over a wave timescale (a few periods) is performed so that

$$\langle u \rangle \rightarrow \mathbf{u} \qquad (3a)$$

$$\langle p \rangle \rightarrow p, \qquad (3b)$$

where (as noted below) the assumption is made that the wave velocities are much larger than the mean velocities. Then the various terms in (2) must be transformed in a dynamically consistent manner. This was done by Huang (1979), who obtained the following equation for the velocity:

$$\frac{\partial \mathbf{u}}{\partial t} + \nabla \frac{1}{2} \mathbf{u}^2 + (\omega + f\mathbf{k}) \times (\mathbf{u} + \mathbf{u}_s)$$

$$= -\frac{\nabla p}{\rho} + \nu_e \nabla^2 \mathbf{u}, \quad (4)$$

---

[1] For purposes of this paper, only the vertical component of the planetary vorticity is considered, so that the cell structure depends only on their orientation relative to the wind and waves, not on their geographic orientation.

where $\mathbf{u}_s$ is the Stokes drift, a Lagrangian drift that arises from the velocity at the crest of the wave being larger than that in the trough (given irrotational surface gravity waves). When averaged over a wave period following a water particle this difference gives rise to a mean drift. Equation (4) is derived under a number of assumptions:

1) The velocities associated with the Langmuir cells are considered to be small (order ϵ, the wave slope) in comparison with the wave orbital velocities.

2) The cells evolve on timescales that are large ($1/\epsilon^2$) in comparison with the wave period.

3) The eddy viscosity and Coriolis force enter the equations at $O(\epsilon^2)$. This is necessary in order to allow the nonlinear stresses associated with the cells to be the same size as the Coriolis force and the transport of momentum by small-scale diffusion.

4) The mixing coefficient within the mixed layer is constant. This is an oversimplification: when the wind is strong and the surface waves are breaking, the mixing coefficient must be larger near the surface (Agarwal et al. 1992). The mixing coefficient should be interpreted as setting the layer-averaged level of turbulent mixing. A consensus on how to consistently describe the development of both the turbulence and the Langmuir cells has not yet emerged.

5) The surface waves are represented as a constant-amplitude infinite-length wave train. This may result in incorrect representation of the total Lagrangian momentum associated with the wave field (McIntyre 1981) whose possible effects will be discussed in section 8.

A frequently asked question is why the Stokes drift only appears in the vortex tipping term and not elsewhere in (4). Why, for example, can the Stokes drift not be advected by vertical velocities? The simplest answer is that the Stokes drift is a wave quantity and so is trapped to the surface gravity waves by the pressure field. The following section provides a qualitative explanation of how this trapping occurs [for a rigourous derivation, the reader is advised to consult Huang (1979) or Gnanadesikan (1994)].

Vertical velocities associated with Langmuir cells can of course advect the velocities associated with the surface waves. However the wave velocities are associated with a pressure field, and pressure fluctuations that arise from the interactions between the $O(\epsilon^2)$ "mean" flows and the $O(\epsilon)$ wave orbital velocities act to counteract such advection. The following example illustrates how this occurs. Imagine that along some y-z plane (which might correspond to an upwelling zone in a Langmuir cell) there is a mean upwelling velocity w_{up} and a wave train propagating in the $+y$ direction with velocity field, as illustrated in Fig. 4. For simplicity, assume that the velocity field associated with the waves is given by
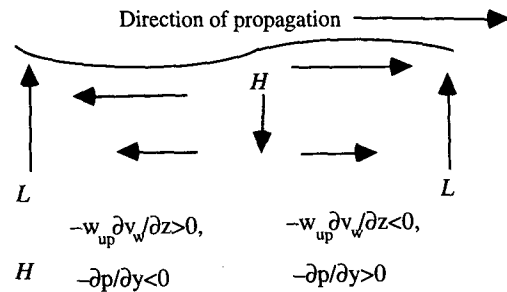

FIG. 4. Illustration of how the velocity field and pressure field associated with the waves interact with the mean vertical velocity in an upwelling zone. Under the forward face of the waves, the mean upwelling and the upwelling due to the waves add. This results in a lower pressure (shown by L). Under the trailing face of the wave, the mean upwelling velocity reduces the downwelling velocity associated with the waves resulting in a higher pressure (denoted by H). Then under a wave crest, the deceleration due to the mean velocity advecting slower-moving water upward is balanced by a pressure-driven acceleration. The same counterbalancing effect occurs under wave troughs.

$$(u_w, v_w, w_w)$$

$$= a_w \sigma e^{k_w z}(0, \cos(k_w y - \sigma t), \sin(k_w y - \sigma t)), \quad (5)$$

where k_w is the wavenumber, σ the frequency, and a_w the amplitude of the surface gravity wave train. Assuming that the wave orbital velocities are larger than the mean upwelling velocity, to first order the particle motion is then

$$(x, y, z) = (x_0, y_0, z_0)$$

$$+ a_w e^{k_w z_0}(0, -\sin(k_w y - \sigma t), \cos(k_w y - \sigma t)). \quad (6)$$

Then following a particle over a wave period and denoting the average over this period by angle brackets, the Coriolis force caused by the wave orbital velocity,

$$fv_w = f\left(v_w + (y - y_0)\frac{\partial v_w}{\partial y} + (z - z_0)\frac{\partial v_w}{\partial z}\right.$$

$$\left. + \text{ higher order terms}\right)\Bigg|_{(y_0, z_0)}, \quad (7)$$

has a nonzero average when (5) and (6) are substituted into (7). Letting the average over a wave period be denoted by angle brackets,

$$\langle fv_w \rangle = fk_w a_w^2 \sigma e^{2k_w z_0} = fv_s(z_0). \quad (8)$$

This force arises because (in the Northern Hemisphere) the Coriolis force to the right of the axis of wave propagation is larger at the crest of the wave than the Coriolis force to the left of the axis of wave propagation at the trough of the wave. Thus, during a single wave

cycle a water particle at a mean depth z_0 receives a net Coriolis acceleration. Similarly,

$$w_{up} \frac{\partial v_w}{\partial z} = w_{up} \left(\frac{\partial v_w}{\partial z} + (y - y_0) \frac{\partial^2 v_w}{\partial y \partial z} \right.$$
$$\left. + (z - z_0) \frac{\partial^2 v_w}{\partial z^2} + \cdots \right) \Bigg|_{(y_0, z_0)} \quad (9)$$

can be shown to have a nonzero average that goes as $\frac{1}{2} w_{up} \partial v_s / \partial z$. However, unlike the wave–planetary vorticity interaction term in (8), the wave–upwelling interaction term in (9) creates a pressure gradient. Underneath the forward face of the wave, the upwelling velocity is increased by w_{up}, while under the trailing face of the wave, the downwelling velocity is decreased by w_{up}. This means that under the forward face of the wave the total kinetic energy is larger while under the trailing face of the wave the total kinetic energy is smaller. By Bernoulli's law, this means that under the forward face of the wave the pressure is smaller than under the trailing face of the wave. The resulting horizontal pressure gradient goes as

$$-\frac{1}{\rho} \frac{\partial p}{\partial y} = a_w \sigma^2 e^{k_w z_0}(0, \sin(k_w y - \sigma t),$$
$$-\cos(k_w y - \sigma t)) + \frac{\partial}{\partial y} (w_{up} w_w), \quad (10)$$

consisting of a term due to the waves only and a term due to the wave–current interaction. For a wave field that is irrotational to first order, the wave–current interaction term balances the advection term in (9). All other terms involving shears in the wave velocities are balanced in the same way and so do not enter the averaged equations (4).

The equations for two-dimensional Langmuir cells may then be derived as follows. Suppose that the cells are invariant in the $+y$ direction (all terms in the averaged equations that have $\partial/\partial y$ in them are zero) and that the following nondimensionalizations are made:

$$La = \frac{\nu_e}{a_w^2 \sigma} \quad F = \frac{f}{k_w^2 a_w^2 \sigma} \quad (11a)$$

$$k_w^{-1}(x, y, z) = (x, y, z) \quad (11b)$$

$$(k_w a_w) 2 \frac{\sigma}{k_w} (u, v, v_s, w) = (\prime, \prime, \prime_{,}, \prime) \quad (11c)$$

$$\frac{1}{k_w^2 a_w^2 \sigma} t = \prime, \quad (11d)$$

where ν_e is the eddy viscosity and f is the Coriolis parameter. Here La is the Langmuir number and serves as a scale for the strength of diffusion, and F is a scaled Coriolis parameter. The lowercase script quantities are dimensional, with (11b–d) giving the conversion from

dimensional to nondimensional variables. Taking the curl of (4) and applying (11) yields the following equation for the vorticity Ω parallel to the cell axis ($\Omega = \partial u / \partial z - \partial w / \partial x$):

$$\frac{\partial \Omega}{\partial t} + (u + u_s) \frac{\partial \Omega}{\partial x} + w \frac{\partial \Omega}{\partial z}$$
$$= F \frac{\partial}{\partial z} (v + v_s) + \frac{\partial v_s \partial v}{\partial z \partial x} + La \nabla^2 \Omega. \quad (12)$$

Vorticity along the cell axis is thus advected by cross-stream Eulerian flows and Stokes drifts, created as the alongcell Eulerian shear and alongcell Stokes drift shear tilts vertical filaments of planetary vorticity and as the alongcell Stokes drift shear tilts vertical filaments of relative vorticity. The vorticity is diffused assuming a constant diffusive coefficient. The alongcell velocity equation is then given by

$$\frac{\partial v}{\partial t} + (u + u_s) \frac{\partial v}{\partial x} + w \frac{\partial v}{\partial z} = -F(u + u_s) + La \nabla^2 v.$$
$$(13)$$

Like the vorticity, the alongcell velocity can be advected by crosscell Eulerian flows and Stokes drifts. Again, the crosscell Stokes drift adds a new body force due to the wave–Coriolis force interactions outlined in (8). Since $\partial v / \partial y = 0$, the continuity equation may be satisfied by defining a streamfunction ψ:

$$\Omega = \nabla^2 \psi \quad (14a)$$

$$\frac{\partial \psi}{\partial x} = -w, \quad \frac{\partial \psi}{\partial z} = u. \quad (14b)$$

The boundary conditions on momentum are set as follows. Because the bottom of the mixed layer can be taken as a barrier to the propagation of subinertial energy (Weller 1981), the stress at the layer base was set to zero so that

$$\frac{\partial v}{\partial z} = \Omega = w = 0 \quad \text{at} \quad z = -D. \quad (15)$$

This bottom boundary condition is an idealization. A more realistic condition would be to relax the no-stress condition so as to permit interactions between the mixed layer and the main thermocline. However, since it is unclear how to define such relaxation of the boundary conditions, this was not done. The flux of momentum is set on the upper boundary:

$$\frac{\partial v}{\partial z} = \frac{\tau}{\rho La} \cos(\alpha) \quad \text{at} \quad z = 0 \quad (16a)$$

$$\Omega = \frac{\tau}{\rho La} \sin(\alpha) \quad \text{at} \quad z = 0. \quad (16b)$$

In the real ocean, stratification can play an important role in changing the mixed layer depth and suppressing

Langmuir circulations (Gnanadesikan 1994). However, because the eddy viscosity is constant, the equations cannot model a steady-state mean thermocline and mixed layer without prescribing unrealistically large heat fluxes within the thermocline. As a result, interactions between the mixed layer and thermocline are not considered in detail in this paper, which focusses instead on the structure of the Ekman spiral within the unstratified mixed layer.

The instability of the mean Ekman spiral, which leads to the generation of Langmuir cells, is solved for by assuming that the mean flow is initially equal to that in the absence of Langmuir circulation with some small perturbation that varies in time and space:

$$\psi = \Psi_0(z) + \Delta\psi'(x, z, t) + \text{higher-order terms}$$

(17a)

$$V(z) = V_0(z) + \Delta v'(x, z, t) + \text{higher-order terms},$$

(17b)

where Δ is a small number. Expanding in Δ, the solution to zeroth order is one for which

$$-F\frac{\partial}{\partial z}(v_s + V_0) = \text{La}\frac{\partial^3 U_0}{\partial z^3}$$

(18a)

$$F(u_s + U_0) = \text{La}\frac{\partial^2 V_0}{\partial z^2}.$$

(18b)

The velocity structure given by these equations is solved for in section 3.

At first order in Δ, the equations are then

$$\frac{\partial\Omega'}{\partial t} + (U_0 + u_s)\frac{\partial\Omega'}{\partial x} + w'\frac{\partial\Omega_0}{\partial z}$$

$$= F\frac{\partial v'}{\partial z} + \frac{\partial v_s\partial v'}{\partial z\partial x} + \text{La}\nabla^2\Omega'$$

(19a)

$$\frac{\partial v'}{\partial t} + (U + u_s)\frac{\partial v'}{\partial x} + w'\frac{\partial V_0}{\partial z} = -Fu' + \text{La}\nabla^2 v'.$$

(19b)

By expanding v' and ψ' in terms of sinusoidal basis functions that satisfy the boundary conditions on velocity, the instability problem can be cast as a linear eigenvalue problem in terms of the coefficients of the basis functions [e.g., Gottleib and Orzsag (1977); see appendix section b(1) for a detailed explanation of how this is done using a Galerkin approximation].

In addition to the Galerkin procedure that formally models the equations of motion, this paper also considers some models that approximate the equations of motion. This is done so as to identify important physical parameters and to include or exclude various physical processes. These models are used to interpret the results of section 4. The first approximate model is a truncated Fourier series:

$$\psi(x, z, t) = \psi_0 e^{\gamma t} \sin(kx) \sin(\pi z/D')$$

$$+ \psi_1 e^{\gamma t} \cos(kx) \sin(2\pi z/D') + \Psi_0(z),$$

$$z > -D' \quad (20a)$$

$$v(x, z, t) = v_0 e^{\gamma t} \cos(kx) \sin(\pi z/D')$$

$$+ v_1 e^{\gamma t} \sin(kx) \sin(2\pi z/D') + V_0(z),$$

$$z > -D' \quad (20b)$$

$$\psi = \Psi_0(z) \quad V = V_0(z), \quad z < -D', \quad (20c)$$

where D' is the maximum penetration depth of the cells. This truncation does not satisfy the boundary conditions on velocity except when La = 0. For small values of La, however, it does closely approximate the shape of the most unstable mode while keeping the problem simple enough to obtain an analytic solution for the growth rate. As noted in Gnanadesikan (1994), truncated models of this type are inaccurate in those cases when they fail to reproduce the structure of the unstably growing cells.

In addition to the truncated model, two modified spectral instability codes are also used to look at the importance of various processes for causing instability. The first code computes the instability of the equilibrium velocity profile as though the Coriolis force does not act on the cells but does act on the background flow. This is not, strictly speaking, a well-posed problem.[2] The purpose of using the modified code for such a scenario is to diagnose the importance of Ekman instability. In this instability mechanism, cells change the curvature of the mean alongcell velocity gradient. These perturbations in velocity curvature are then turned by the Coriolis force to reinforce the cells (Gammelsrød 1975; Lele 1985). If the growth rate of cells in the absence of Coriolis force is smaller than the growth rate in the presence of Coriolis force, Ekman instability probably contributes to cell growth. If the growth rate does not change significantly, Ekman instability most likely does not contribute. If the growth rate in the absence of Coriolis force is larger, the Coriolis force is acting to suppress the instability. The growth rates calculated from this code are referred to as being computed "in the absence of Coriolis forces." A second modified instability code examines the importance of shear instability by expanding the streamfunction alone [see appendix section b(2) for details]. The growth rates from this code will be referred to as due to "shear instability alone."

---

[2] In the limit when the growth rate of the most unstable mode γ is large in comparison with the scaled Coriolis frequency one can rescale the equations in terms of F/γ to obtain a formally valid expression for the growth rate. However, in many of the cases for which this procedure is used, the growth rates are of the same order as the Coriolis frequency, so that even this procedure is not formally valid.

In the presence of finite-amplitude Langmuir cells Eqs. (12)–(14) can be integrated using a finite-difference code. Gnanadesikan (1994) developed a simple finite-difference code, which is used in section 7 to evaluate how Langmuir cells at finite amplitude actually modify the Ekman spiral. A brief description of the finite-difference code is given in appendix section c.

3. The Ekman response in the presence of waves

To understand how instabilities act to modify the mean profile of velocity, it is necessary to solve for that profile in the presence of waves. Integrating (18a) with respect to z and defining the complex velocity and Stokes drift profiles:

$$W(z) = U(z) + iV(z) \qquad (21a)$$

$$W_s(z) = u_s(z) + iv_s(z) \qquad (21b)$$

yields the following equation for the steady-state complex velocity vector:

$$iF(W_s + W) = \text{La}\frac{\partial^2 W}{\partial z^2}. \qquad (22)$$

In the absence of waves ($W_s = 0$), this equation has the following solution:

$$W_{\text{Ek}} = \frac{\tau}{\text{La}(1+i)}\frac{1}{e^{(1+i)D/\delta} - e^{-(1+i)D/\delta}}$$

$$\times (e^{(1+i)(z+D)/\delta} + e^{-(1+i)(z+D)/\delta}), \qquad (23)$$

where $\delta = \sqrt{2\text{La}/F}$ is the Ekman depth. The presence of waves, however, introduces an additional term, an Eulerian return flow whose total mass transport balances that associated with the Stokes drift. This flow is driven by a body force associated with the wave–Coriolis force interaction. For purposes of this paper, the surface stress and wave field are taken to be separable. In reality this is probably not the case [see Weber and Melsom (1993) for a discussion] since the stress may well depend on the wave field. However, such dependence will merely lead to a different value of surface stress in (23) and will not alter the wave–Coriolis force term. The wave-driven return flow W_{wave} may be solved for using the method of Green's functions:

$$W_{\text{wave}}(z) = \int_{-D}^{0} G(z, z_0)W_s(z_0)dz_0, \qquad (24)$$

where G is given by

$$G(z, z_0) = A_+(z_0)(e^{(1+i)z/\delta} + e^{-(1+i)z/\delta}), \quad z > z_0 \qquad (25a)$$

$$G(z, z_0) = A_-(z_0)(e^{(1+i)(z+D)/\delta} + e^{-(1+i)(z+D)/\delta}), \quad z < z_0 \qquad (25b)$$

$$A_+(z_0)$$

$$= \frac{1}{2}\frac{\delta}{1+i}\frac{e^{(1+i)(z_0+D)/\delta} + e^{-(1+i)(z_0+D)/\delta}}{e^{-(1+i)D/\delta} - e^{(1+i)D/\delta}} \qquad (25c)$$

$$A_-(z_0) = \frac{1}{2}\frac{\delta}{1+i}\frac{e^{(1+i)z_0/\delta} + e^{-(1+i)z_0/\delta}}{e^{-(1+i)D/\delta} - e^{(1+i)D/\delta}}. \qquad (25d)$$

The structure of the return flow is strongly dependent on the nondimensional Ekman number

$$\text{Ek} = \frac{\text{La}}{F} = \frac{\nu_e k_w^2}{f}$$

$$= 2\pi^2 \left(\frac{\text{Ekman depth}}{\text{wavelength of surface gravity waves}}\right)^2, \qquad (26)$$

where k_w is the wavenumber of the driving waves. When Ek is small, the Eulerian return flow essentially balances the Stokes drift at each depth. When it is large, the return flow is smoothed out over depths comparable to an Ekman depth (or if it is smaller, the mixed layer depth). Figure 5 shows the structure of the Eulerian return flow driven by a Pierson–Moskowitz (1964) wave spectrum, for which

$$v_s(z) = \int_{f=0}^{\infty}\frac{5}{f^2}\exp\left(-1.25\frac{1}{f^4}\right)\exp(2f^2z)df, \qquad (27)$$

where f is a dummy variable denoting the wave frequency. Calculations are presented given a layer depth of 4, no surface stress, and Ek ranging from 0.01 to 100. In the midlatitude open ocean, the wave amplitude is large ($a_w \sim 1$ m), the wavelengths are quite long ($k_w^{-1} \sim 0.05$–0.1 m^{-1}), and the eddy viscosities are fairly high (0.01–0.05 m s^{-1}). In such cases Ek is of order 1, and La is of order 0.01. The range of cases shown here is thus reasonable for oceanic Ekman spirals.

The results presented above asymptote to those of previous investigators (Hasselmann 1970; Huang 1979; Weber 1983; Weber and Melsom 1993; Xu and Bowen 1994) when identical assumptions (generally some subset of the following: deep water, monochromatic waves, and zero viscosity) are made.[3]

4. The instability of the Ekman spiral to Langmuir circulations

The Ekman spiral in the presence of surface gravity waves can be strongly unstable to two-dimensional roll vortices. This section studies the instability of Ekman spirals given a range of Ek from 0.01 to 100 and a range

---

[3] The first three authors, for example, all predict a mean inviscid (La = 0) flow in deep water that is equal and opposite to the Stokes drift, as does this work.
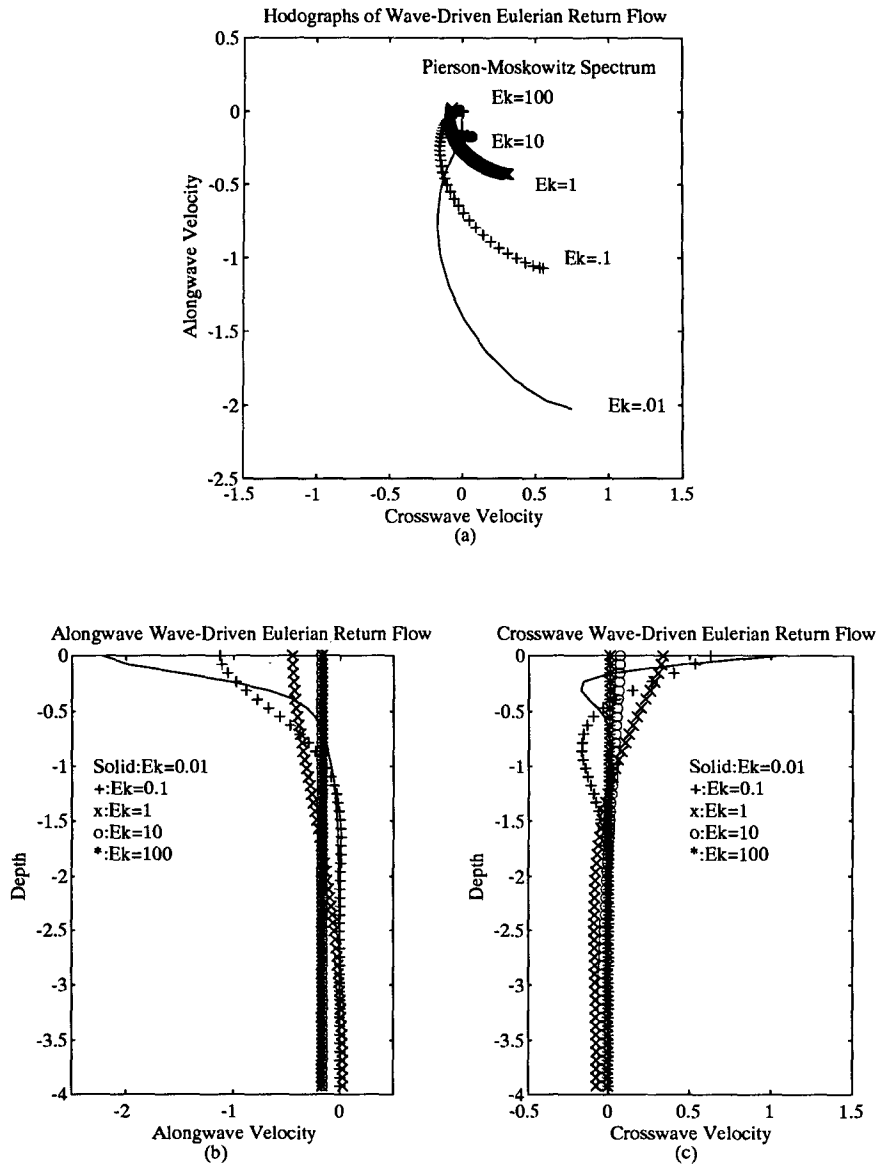
Hodographs of Wave-Driven Eulerian Return Flow

FIG. 5. Return flow driven by a Pierson–Moskowitz spectrum for different values of Ek, Solid: Ek = 0.01, +: Ek = 0.1, ×: Ek = 1, O: Ek = 10, *: Ek = 100. (Note: the last two flows are essentially identical.) (a) Hodograph of the return flow. (b) Vertical profile of the alongwave component of the return flow. (c) Vertical profile of the cross-wave component of the return flow. Velocity is nondimensionalized by the Stokes drift scale $k_w a_w^2 \sigma$.

of La from 0.001 to 0.1. This spans a range of La and Ek expected for the open ocean. In all of the profiles studied here, the waves are taken to be parallel with the wind [see Rieder et al. (1994) for a verification of this common assumption]. The nondimensional surface Eulerian shear is always set to 1, so the stress and Langmuir number are linearly related. This is done so that differences in growth rate are due to differences in the *structure* of the current profile, rather than being caused by differences in the strength of the shear. Such a linear relationship does not exist in the real world. The mixed

layer depth is set to 4, so the Stokes drift is felt only over the top one-fourth of the mixed layer.

As demonstrated in section 3, the velocity structure can depend on the presence of waves. Figure 6 shows hodographs of the Ekman spiral with (solid) and without (dashed) surface gravity waves as a function of La and F. As in section 3, the structure of the Ekman spiral is a function of Ek $=$ La$/F$ with constant values of Ek running from the upper left to the lower right of the figure. The presence of waves modifies the hodographs greatly when Ek is small (lower left-hand corner), in-

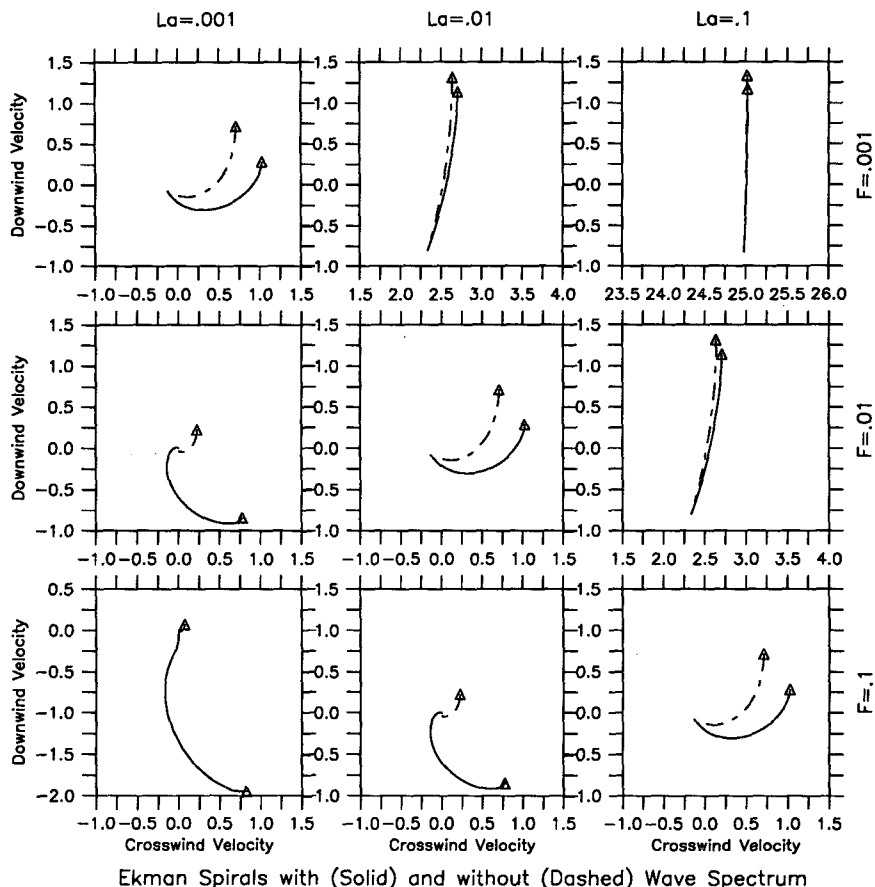Ekman Spirals with (Solid) and without (Dashed) Wave Spectrum

FIG. 6. Hodographs of the Eulerian velocity profile without waves (dashed) and with waves given by a Pierson–Moskowitz wave spectrum, assuming a nondimensional layer depth of 4 and a surface Eulerian shear of 1. The surface velocities are indicated by the open triangles. The profiles in the absence of waves are computed from Eqs. (23), those in the presence of waves by adding the solutions from Eqs. (24) and (25) to that in the absence of waves. The assumption is made that all the Ekman flow is carried within the layer.

troducing a strongly sheared Eulerian return flow. When Ek is large (upper right), the presence of waves changes the mean flow slightly, producing an offset in the transport, but does not greatly change the structure of the shear.

The growth rate of the fastest-growing unstable mode as a function of angle of cell orientation and horizontal wavenumber is shown in Fig. 7. Growth rates were computed using the Galerkin code described in appendix section b(1). The growth rates depend on the horizontal wavenumber, the angle of cell orientation, the Langmuir number La, and the scaled Coriolis frequency F. The fastest-growing cells have growth rates of $O(0.1-1)$. In all but the lower row, the growth rates are much larger than the scaled Coriolis frequency, implying that the Ekman spirals in Fig. 6 are strongly unstable to Langmuir cells and thus will most likely not be seen in the real world.

The angle at which the cells are oriented depends on the current profile, which is in turn a function of Ek.

When Ek is large, the Eulerian shear is essentially parallel with the wind and waves and the cell axis is oriented alongwind. As Ek decreases (moving from upper right to lower left), the Eulerian shear moves off to the right of the wind, as does the axis of cell orientation. The relationship between the cell axis and the direction of the Eulerian shear is explored in more detail in the following section.

Diffusion also plays an important role in determining the growth rates. Given a constant current profile (constant Ek), the maximum growth rate is a strong function of the Langmuir number La. Increasing La, corresponding to increasing the effect of diffusion, reduces the growth rate and suppresses growth at large wavenumbers (small wavelengths).

It has long been known (Brown 1970) that the Ekman spiral can become unstable to roll vortices. It is important to ask whether the presence of waves is necessary for strongly growing vortices to appear on the Ekman spiral. If the Stokes drift is set equal to zero, the same
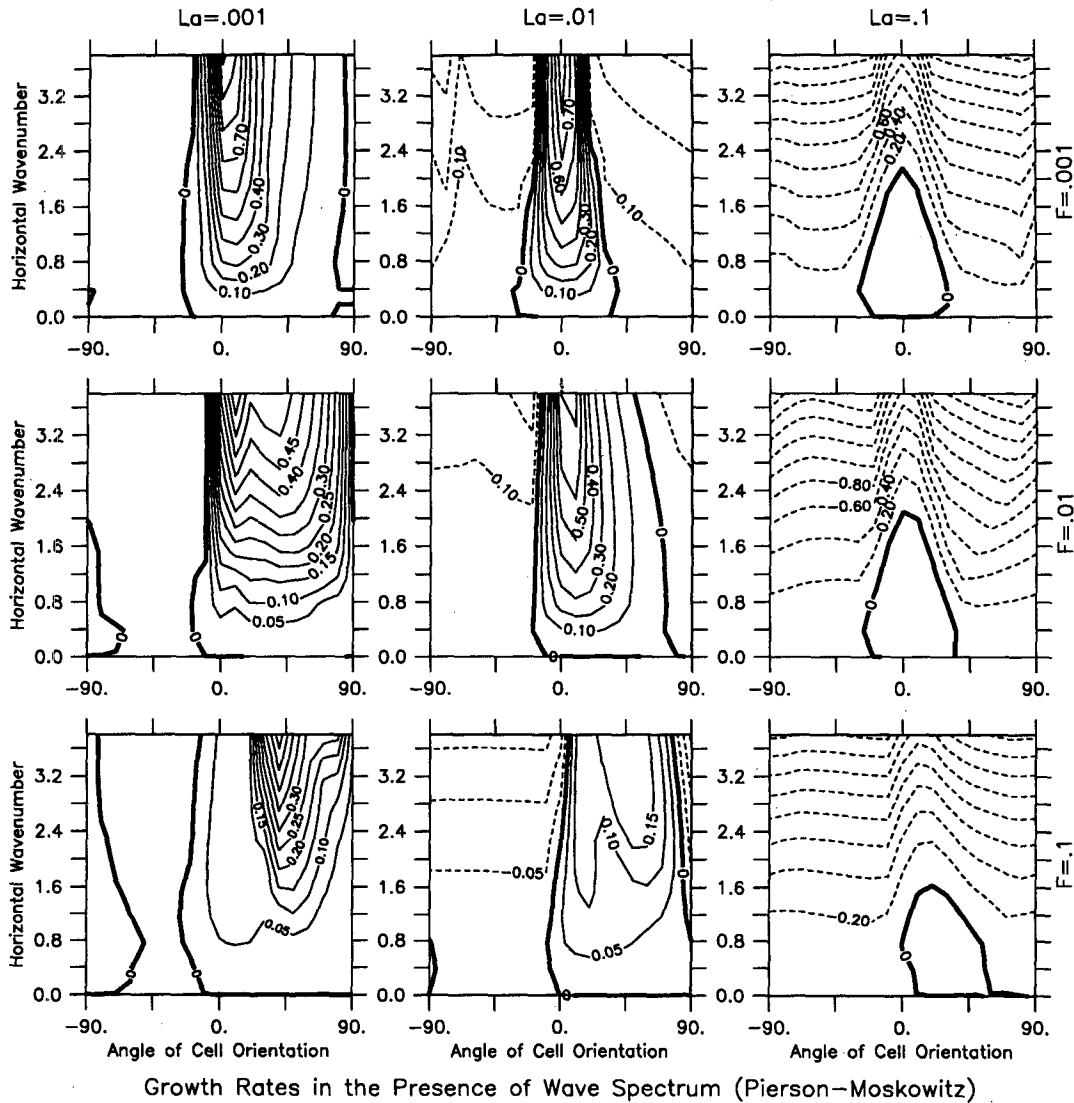
Growth Rates in the Presence of Wave Spectrum (Pierson–Moskowitz)

FIG. 7. Growth rate of the most unstable mode as a function of horizontal wavenumber (vertical axis) and angle of orientation α of the cell axis relative to the wind (horizontal axis, 0 is parallel with the wind and waves, ±90 is perpendicular to the wind and waves). Waves are given by a Pierson–Moskowitz spectrum. Growth rates for $\alpha \pm 180$ are the same as those for α. Negative contours are dashed. Growth rates were calculated using a 40-mode Galerkin code with sinusoidal basis functions. Top left: $F = 0.001$, La = 0.001. Top center: $F = 0.001$, La = 0.01. Top right: $F = 0.001$, La = 0.1. Middle left: $F = 0.01$, La = 0.001. Middle right: $F = 0.01$, La = 0.1. Bottom left: $F = 0.1$, La = 0.001. Bottom center: $F = 0.1$, La = 0.01. Bottom right: $F = 0.1$, La = 0.1.

Galerkin code used to calculate the growth rates in Fig. 7 can be used to calculate the Ekman spiral without waves. The pattern of growth when there are no waves in the problem is shown in Fig. 8. The presence of waves substantially alters the stability of an Ekman spiral. When Ek is large, the Ekman spiral is stable in the absence of waves and strongly unstable in the presence of waves. For the range of cases shown, the growth rates in the presence of waves are all larger than the Coriolis frequency. In the absence of waves, there are some unstable two-dimensional disturbances when Ek is sufficiently small. The growth rates of these disturbances, however, are at most one-third the Coriolis frequency, in marked contrast to those in the presence of waves. In the absence of waves, the disturbances are well off to the right of the wind (45–70 deg). By contrast, Langmuir cells in the open ocean are generally aligned within about 15 deg to the wind (Faller 1964), as is the case when waves are present. Last, with the exception of the lowest value of Ek (0.01 in the lower left-hand corner), the fastest-growing vortices when waves are not present has a wavelength much larger than the e-folding scale
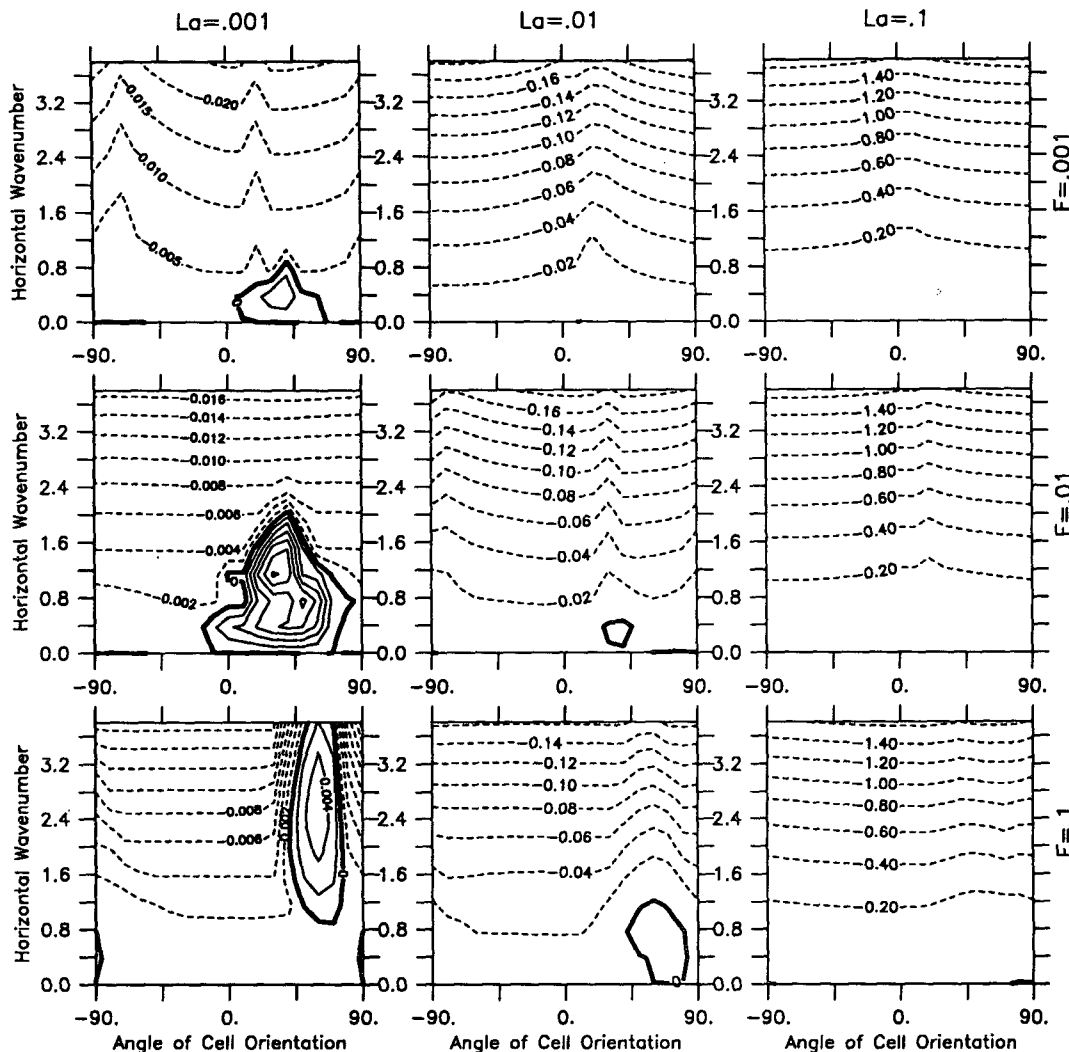
Growth Rates in the Absence of Surface Gravity Waves

FIG. 8. Same as Fig. 7 but assuming that waves affect neither the current profile,
nor do they drive Langmuir cells through wave–current interaction.

of the waves. For open-ocean conditions, this implies that the first cells to appear would have wavelengths of order 50–100 m. By contrast, in the presence of waves, the fastest-growing cells are much smaller as seen in the field (Leibovich 1983).

The results displayed in Figs. 7 and 8 raise a number of questions:

1) What are the principal processes responsible for driving the instability? In addition to Craik–Leibovich instability, surface gravity waves may also increase the effect of shear instability centering around inflection points in the velocity profile (Brown 1970; Mourad 1995) or the increased shear in the Eulerian return flow may change the effect of Ekman instability (Gammelsrød 1975).

2) What determines the size of the growth rate and the angle of orientation of the cells? Previous work has assumed that the cell axis and Eulerian shear are all parallel. This is clearly not true in the presence of Coriolis forces. In fact, for very small Ek, cells lying parallel to the wind are only very weakly unstable. These questions are considered in more detail in the following section.

5. Langmuir cells in nonparallel flow

a. *Setting the angle of maximum instability: Crosscell shear and wave–current interaction*

The following processes can all play a role in the dynamics of two-dimensional roll vortices:

1) Wave–current interaction. This forces cells when the product of the projection of the Stokes drift shear and Eulerian shear on the axis of cell orientation is positive.

2) Tilting of cells by crosscell shear. This tends to reduce the growth rate.

3)* Diffusion. For the cases presented here, diffusion reduces the growth rate. When layers with strong Stokes drift shear and Eulerian shear are not collocated, however, this is not necessarily the case.

4) Shear instability centered around inflection points in the velocity profile. This mechanism is thought to be responsible for the instability of the atmospheric Ekman layer (Brown 1970).

5) Coriolis effects. These can either induce instability (Gammelsrød 1975) or suppress it.

This subsection focuses on the tradeoff between minimizing the crosscell shear and maximizing the wave–current interaction. In order to do this a simplified scenario (shown in Fig. 9) is considered. Both the Stokes drift and Eulerian shears are assumed to be constant and to lie along axes that are separated by an angle θ. The cells lie along some axis α relative to the Stokes drift shear. If F and La are 0, the truncation in (20) may be substituted into (12) and (13), and the instability problem may be reduced to the following eigenvalue problem:

$$
\begin{pmatrix}
\gamma & \sigma_{shear}^{(1)} & -\dfrac{k}{k^2+(\pi/D')^2}\hat{V}_{sz}^{(1)} & 0 \\
-\sigma_{shear}^{(2)} & \gamma & 0 & \dfrac{k}{k^2+4(\pi/D')^2}\hat{V}_{sz}^{(2)} \\
-k\hat{V}_z^{(1)} & 0 & \gamma & \sigma \\
0 & k\hat{V}_z^{(2)} & -\sigma & \gamma
\end{pmatrix}
\begin{pmatrix}
\psi_0 \\
\psi_1 \\
v_0 \\
v_1
\end{pmatrix} = 0, \qquad (28)
$$

where

$$
\hat{V}_z^{(1,2)}(D') = \frac{2}{D'}\int_{-D'}^{0}\frac{\partial V_0}{\partial z}\sin^2\!\left(\frac{(1,2)\pi z}{D'}\right)dz
$$

$$
= \left|\frac{\partial V}{\partial z}\right|\cos(\theta-\alpha) \qquad (29a)
$$

$$
\hat{V}_{sz}^{(1,2)}(D') = \frac{2}{D'}\int_{-D'}^{0}\frac{\partial v_s}{\partial z}\sin^2\!\left(\frac{(1,2)\pi z}{D'}\right)dz
$$

$$
= \left|\frac{\partial V_s}{\partial z}\right|\cos(\alpha) \qquad (29b)
$$

$$
\sigma = \frac{2k}{D'}\int_{-D'}^{0}\left(\frac{\partial\Psi_0}{\partial z}+u_s\right)\sin\!\left(\frac{\pi z}{D'}\right)\sin\!\left(\frac{2\pi z}{D'}\right)dz
$$

$$
= \frac{4}{3\pi^2}kD'\left(\left|\frac{\partial V_s}{\partial z}\right|\sin(\alpha) - \left|\frac{\partial V}{\partial z}\right|\sin(\theta-\alpha)\right) \qquad (29c)
$$

$$
\sigma_{shear}^{(1)} = \frac{k^2+(2\pi/D')^2}{k^2+(\pi/D')^2}\sigma \qquad (29d)
$$

$$
\sigma_{shear}^{(2)} = \frac{k^2+(\pi/D')^2}{k^2+(2\pi/D')^2}\sigma, \qquad (29e)
$$

where the superscripts refer to the vertical wavenumber of the perturbations. Physically, $\hat{V}_{sz}^{(1,2)}$ and $\hat{V}_z^{(1,2)}$ represent the depth-weighted averages of the alongcell Stokes drift and Eulerian shears, respectively, where the weighting function is proportional to the momentum transport carried by Langmuir cells with either one or two maxima in vertical velocity. The frequencies $\sigma_{shear}^{(1)}$, $\sigma_{shear}^{(2)}$, and σ are measures of the effectiveness of the crosscell shear at coupling cells with different vertical wavenumbers. These terms scale as the aspect ratio kD' times the crosscell shear; σ will be referred to as the crosscell tilting frequency.

This simple case is useful because it involves only two physical processes, wave–current interaction and crosscell shear. Shear instability cannot cause instability because the Eulerian shear is constant (Case 1960). Ekman instability cannot occur because $F = 0$. Diffusion does not play a role because La = 0. As such, the constant shear scenario allows the development of an understanding of the two most important physical mechanisms determining the growth rate and orientation of the cells.

Defining

$$
\gamma_I = \left(\frac{k^2}{k^2+(\pi/D')^2}\hat{V}_z^{(1)}\hat{V}_{sz}^{(1)}\right)^{1/2}
$$

$$
= \left(\frac{k^2 D'^2}{k^2 D'^2 + \pi^2}\left|\frac{\partial V}{\partial z}\right|\left|\frac{\partial V_s}{\partial z}\right|\right)
$$

$$
\times \cos(\theta-\alpha)\cos(\alpha)\Big)^{1/2} \qquad (30a)
$$

Stokes Drift   Eulerian Shear
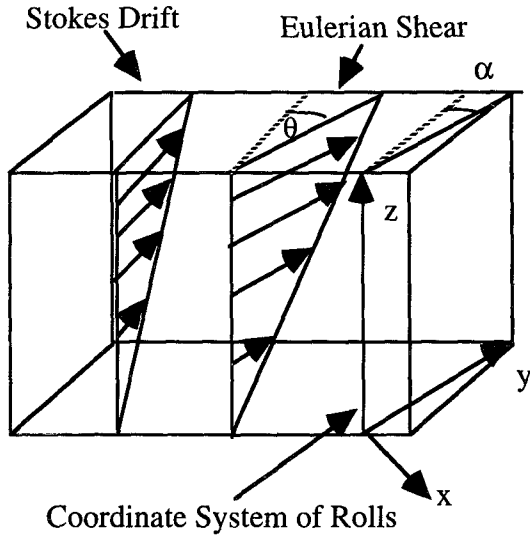

Coordinate System of Rolls

FIG. 9. Schematic of the simplified, linear shear case used to explore the dependence of the angle of cell instability on the separation between the Eulerian and Stokes drift shears.

$$\gamma_1 = \left(\frac{k^2}{k^2 + (2\pi/D')^2} \hat{V}_z^{(2)} \hat{V}_{sz}^{(2)} \right)^{1/2}$$

$$= \left(\frac{k^2 D'^2}{k^2 D'^2 + 4\pi^2} \left| \frac{\partial V}{\partial z} \right| \left| \frac{\partial V_s}{\partial z} \right| \right.$$

$$\left. \times \cos(\theta - \alpha) \cos(\alpha) \right)^{1/2}, \quad (30b)$$

the solution to (29) is given by

$$\gamma^2 = \max(\gamma_1^2 - \sigma^2, \gamma_2^2 - \sigma^2). \quad (31)$$

The truncation is used to approximate the results of the instability code by maximizing γ with respect to D' with all other parameters held fixed.

For the constant shear case in Fig. 9, (31) does an excellent job at predicting both the maximum growth rate and the angle of cell orientation at which that growth rate occurs. Figure 10 shows the growth rate and angle of orientation of the fastest-growing cells as a function of Eulerian shear and θ given constant Stokes drift shear. For constant Eulerian shear, as θ increases, the angle of orientation increases and the growth rate drops. This behavior is identical to that seen in an unstable Ekman spiral, so that understanding the behavior in Fig. 10 can lead to insight about the Langmuir cell orientation and growth rate as a function of Ek. Note that when the Eulerian shear and Stokes drift shear are equal (solid, lines, +-marks) the maximum instability occurs at one-half the separation angle and (31) gives a result identical to the full Galerkin code. When the Eulerian shear is larger than the Stokes drift shear, the angle of maximum instability lies closer to the axis of the Eulerian

shear. This behavior can be explained by considering (31) in detail.

The growth rates predicted by (31) depend on both the strength of the wave–current interaction and the tilting of the cells due to crosscell shear. They depend not only on the structure of the mean flow, but also on the depth of penetration of the cells D'. As shown in Gnanadesikan (1994), the concentration of the wave–current interaction forcing near the oceanic surface results in the depth of penetration being a function of the wavelength. Short-wavelength cells penetrate less deeply into the water column than long-wavelength cells.

For the case at hand, the growth rate is determined by a trade-off between maximizing γ_1 and γ_2 and minimizing σ; γ_1 and γ_2 are maximized when kD' and the product $\cos(\theta - \alpha) \cos(\alpha)$ are maximized. The former occurs when the cells fill the entire domain $(D' = D)$. The latter occurs when $\alpha = \theta/2$, so that the cell axis lies halfway between the Eulerian velocity and Stokes drift. Effectively, maximizing $\cos(\theta - \alpha) \cos(\alpha)$ corresponds to maximizing the ability of the wave–current interaction mechanism in converting a given stress into eddy kinetic energy. Maximizing kD', on the other hand, corresponds to maximizing the efficiency of the released eddy kinetic energy at feeding back on the stress. When kD' is small, most of the released energy in the crosscell direction goes into horizontal rather than vertical motions. For linearly unstable cells, these horizontal velocities do not reinforce the alongcell jets. By contrast, the tilting of the cells by crosscell flow will be small when kD' is small or when the crosscell Lagrangian shear $\partial U^L/\partial z$

$$\frac{\partial U^L}{\partial z} = \left| \frac{\partial V_s}{\partial z} \right| \sin(\alpha) - \left| \frac{\partial V}{\partial z} \right| \sin(\theta - \alpha) \quad (32)$$

is small.

When the Stokes drift and Eulerian shears are equivalent in magnitude, the wave–current forcing is maximized and the crosscell shear is minimized when $\alpha = \theta/2$ so that the growth rate of the fastest-growing mode is

$$\gamma = \left(\frac{k^2 D^2}{k^2 D^2 + \pi^2} \left| \frac{\partial V}{\partial z} \right| \left| \frac{\partial V_s}{\partial z} \right| \right)^{1/2} \cos(\theta/2). \quad (33)$$

When the Stokes drift and Eulerian shears have different magnitudes, the axis of instability lies closer to the larger of the two shears, and the growth rates are smaller than that given by (33).

The dependence of the growth rate and angle of instability on Ek can now be explained. For large Ek, the Stokes drift and Eulerian shears are aligned. Maximizing the forcing on the cells and minimizing the crosscell tilting of the cells requires that the cells be aligned parallel with the Eulerian velocity and Stokes drift shears. As Ek becomes smaller, however, the angle between

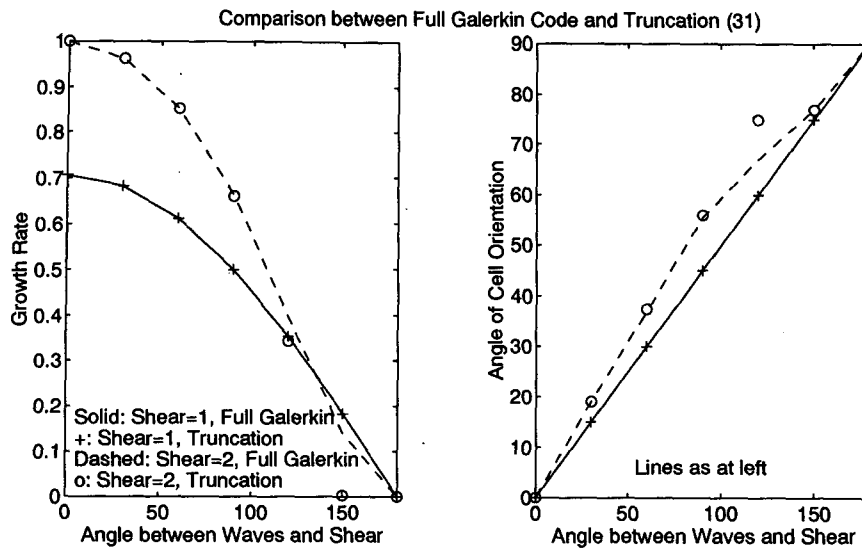Comparison between Full Galerkin Code and Truncation (31)

FIG. 10. Verification of (31) as a predictor of the growth rate for the constant shear case in Fig. 9. Results from (31) are compared with the full Galerkin code for constant Stokes drift shear = 1 and cells with a wavelength twice the water depth; $La = F = 0$. Horizontal axis is θ, angle between the shear and waves. Two values of Eulerian shear are used. Solid: full Galerkin code, Eulerian shear = 1. Dashed: full Galerkin code, Eulerian shear = 2. +: Growth rate from (31) with Eulerian shear = 1. O: Growth rate from (31) with Eulerian shear = 2. Note that the truncation is very close to the full code with the exception of one point. Left: fastest growth rate. Right: angle at which that growth rate occurs. Note that when the two shears are equal, the angle of maximum instability is one-half of the separation angle, while when the Eulerian shear is larger, the angle of instability lies closer to that axis.

the mean Eulerian shear and the mean Stokes drift shear increases and the axis of cell orientation is in between the two. This physical trade-off provides a rationale for Faller's (1964) result that cells in the Northern Hemisphere are oriented off to the right of the wind. Individual cases, however, could behave differently, particularly if the wind is shifting direction or there is swell at some angle to the wind. The key physics (namely the dependence on the angle between Eulerian and Stokes drift shears) is not dependent on whether the wind and waves are aligned.

b. Effects of other instability processes

Although section 5a does give a qualitative explanation for the dependence of growth rate and angle of instability on Ek, it does not provide much insight into how other physical processes affect the instability. This section explores two such questions.

1) How does the presence of Coriolis forces affect the instability? Does it drive Ekman instability, enhancing the growth rates, or does it stabilize two-dimensional instabilities?

2) To what extent does shear instability contribute to Langmuir cell growth?

These questions were approached using the modified Galerkin codes described in appendix section b(2). As

outlined in section 2 and b(2), one of these codes omits the effect of the Coriolis force on the unstable rolls, while the other omits the effects of wave–current interaction on the rolls as well. The codes were run for the three scenarios with $F = 0.01$ presented in Fig. 7 (the central row). The results are presented in Fig. 11. The pattern of growth rates in the absence of Coriolis forces closely resembles that in the presence of Coriolis forces (compare the top and middle rows of Fig. 11). The range of angles over which the Ekman spiral is unstable is somewhat reduced. Away from the instability boundary, however, the magnitude of the growth rate increases in the absence of Coriolis forces over most of the range of parameters shown. Coriolis forces, then, tend to have a damping effect on the most strongly growing Langmuir cells, while destabilizing some marginally stable cells far from the axis of greatest instability.

The angle of maximum instability is also affected by the presence or absence of Coriolis forces. In the absence of Coriolis forces, the angle at which the maximum instability occurs shifts away from the axis along which the Eulerian shear is oriented and closer to the axis of wave propagation. This may be because the Ekman instability mechanism is strongest for cells that are oriented along the axis of the Eulerian shear. In the absence of Coriolis forces, the cells oriented along the axis of Eulerian shear have their growth rates decrease, and the axis of maximum instability shifts closer to

La=.001   La=.01   La=.1

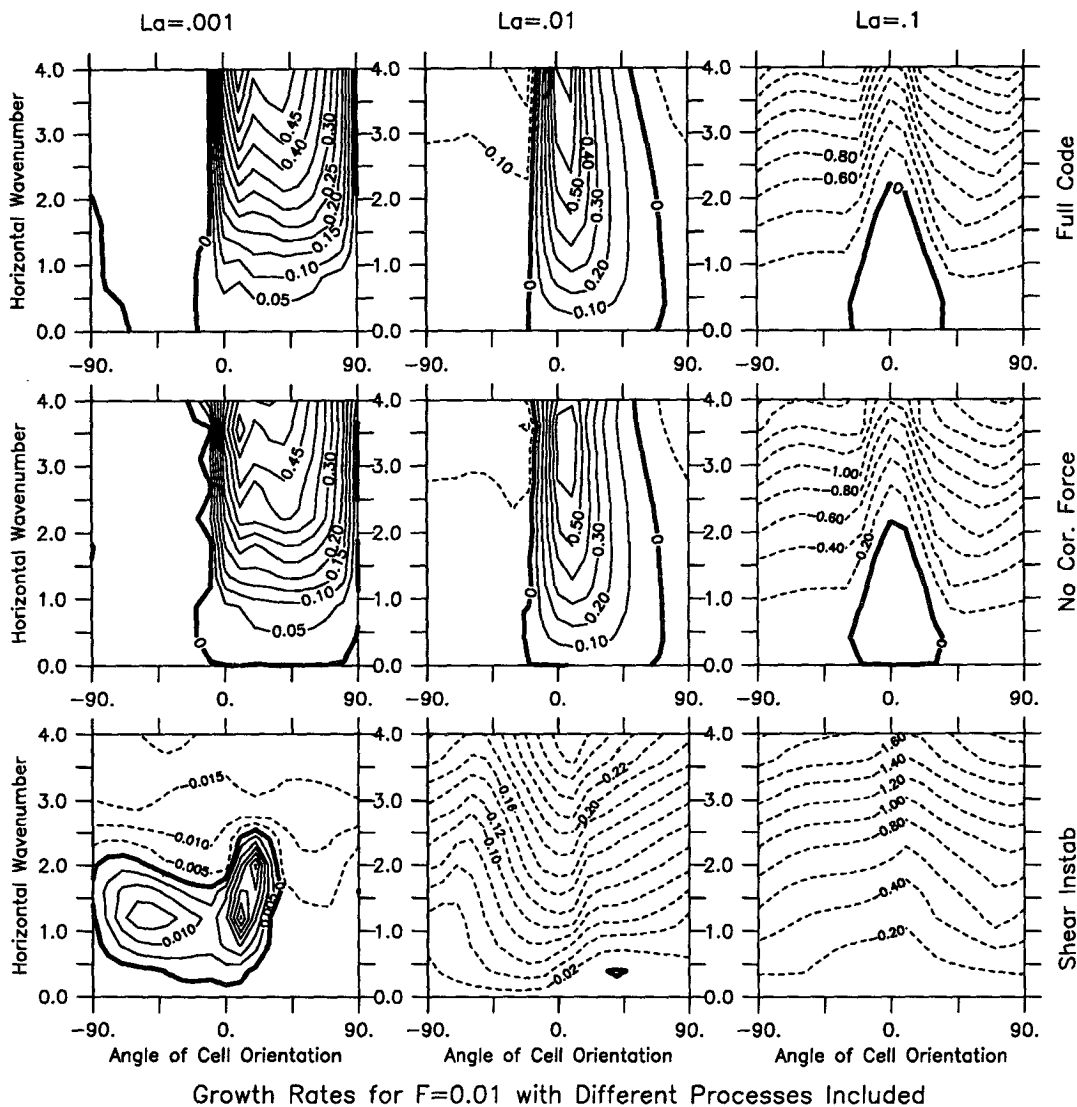Growth Rates for F=0.01 with Different Processes Included

FIG. 11. Growth rates for two-dimensional Langmuir cells with $F = 0.01$ as a function of horizontal wavenumber (vertical axis) and angle relative to the wind and waves (horizontal axis) as in Figs. 7 and 8. Top row reproduces the middle row of Fig. 6 with slightly different vertical axis. Middle row shows the growth rates calculated as if the Coriolis force had no effect on the instability (though it is presumed to have an effect on the mean flow). Ekman instability is thus "turned off" in this case. Note the similarity between the top and middle rows, indicating that Ekman instability is not a dominant process. Bottom row shows the growth rates calculated for two-dimensional shear instability (assuming no effects from either Coriolis forces or Craik-Leibovich interaction). Dashed lines are contours of negative growth rates; solid lines positive growth rates. Note the major differences between top and bottom rows, demonstrating that Craik-Leibovich interaction is a dominant process, more important in setting the growth rates than shear instability.

being midway between the axis of wave propagation and the axis of the Eulerian shear.

Shear instability does not play a critical role in Langmuir cell growth for the cases shown (compare the top and bottom rows of Fig. 11). The growth rates due to shear instability alone are far smaller than those associated with wave–current interaction. Indeed, only for Ek = 0.1 are there significant shear instabilities at all, and even these have relatively small growth rates (only 3 to 4 times the Coriolis frequency and fully an order

of magnitude smaller than those associated with wave–current interaction). In combination, these results support the hypothesis that oceanic Langmuir cells are primarily driven by wave–current interaction, rather than Ekman or shear instability.

6. Instability of the unstratified Ekman spiral during MILDEX

The theoretical discussion developed above is now applied to the example from the Mixed Layer Dynam-
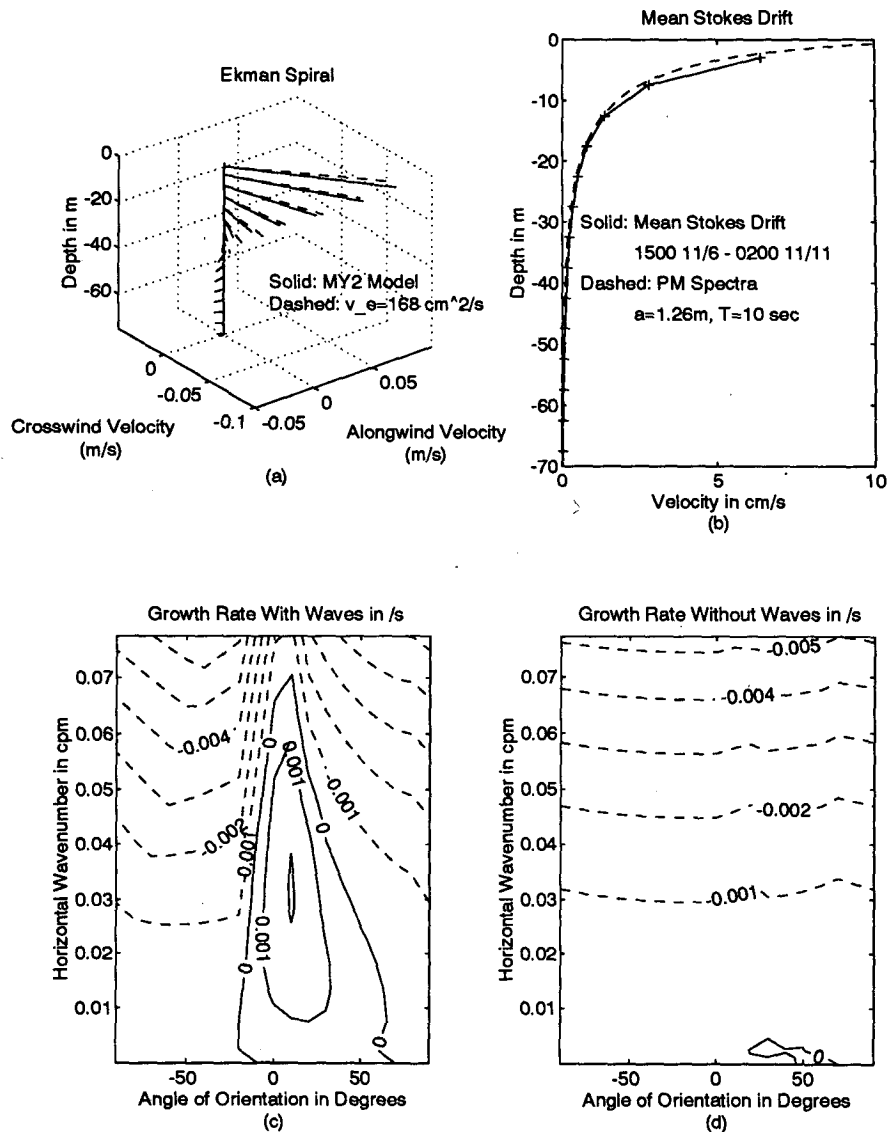
FIG. 12. Instability of the mean Ekman response during MILDEX to Langmuir cells. (a) Ekman spiral predicted using the MY2 model (solid) and using an averaged eddy viscosity of 0.0168 m^2 s^{-1}. (b) Mean Stokes drift calculated using a wavestaff aboard *FLIP* (solid) and fitted using a Pierson–Moskowitz spectrum (dashed) with rms amplitude of 1.26 m and peak period of 10 sec. (c) Growth rate in s^{-1} of the most unstable mode as a function of wavenumber in cpm (vertical) and angle of cell orientation (horizontal) assuming waves act on both the cells and mean flow. Dashed lines are negative contours. (d) Growth rate of most unstable mode assuming waves act on neither the cells nor the mean flow.

ics Experiment (MILDEX) outlined earlier in this paper. This section considers the tendency of the mean profile to become unstable. The approach taken is to compute the instability of the mean Ekman response assuming the cells to be forced by the mean waves and wind stress. This approach has certain limitations. In particular, if Langmuir when cells appear only there is no diurnal restratification, looking at instability of the mean structure will result in Langmuir cells being driven by shears that are not present at the same time

as the cells. It is hoped that by looking at a time period when cells were almost always present such effects will be minimized. Nonetheless, the mean structure may not actually be representative of any specific time.

The Ekman response predicted by the MY2 model is well approximated by assuming a constant eddy viscosity of 0.0168 m^2 s^{-1} (Fig. 12a). The averaged Stokes drift during the high-wave period in MILDEX can be modeled by a Pierson–Moskowitz spectrum that has a peak period T_{peak} of 10 sec and an rms wave
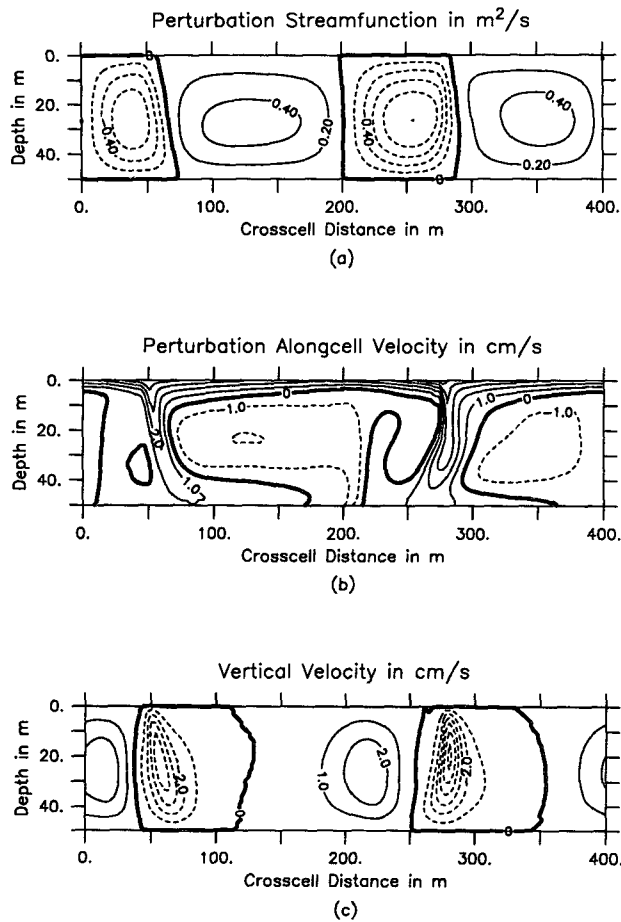
Perturbation Streamfunction in m²/s

(a)

Perturbation Alongcell Velocity in cm/s

(b)

Vertical Velocity in cm/s

(c)

FIG. 13. Modeled mixed layer structure using mean MILDEX parameters after roughly one-dimensional day. (a) Perturbation streamfunction in m² s⁻¹. (b) Alongcell velocity in centimeters per second. Mean over the entire mixed layer has been removed. Solid lines are positive (downwind); dashed lines negative (upwind). (c) Vertical velocity in centimeters per second. Solid lines are positive (up), and dashed lines negative (down).

amplitude of 1.26 m. This implies a characteristic length scale L of 25 m (the inverse wavenumber of a deep water surface gravity wave with a period of 10 s). This in turn implies a Langmuir number of

$$\mathrm{La} = \frac{\nu_e T_{\mathrm{peak}}}{2\pi a^2} = 0.017 \qquad (34)$$

and a scaled Coriolis frequency

$$F = \frac{f T_{\mathrm{peak}} L^2}{8\pi^3 a^2} = 0.051, \qquad (35)$$

where f is the dimensional Coriolis frequency. By applying the mean absolute stress over this time period (0.131 Pa), one can calculate a mean, nondimensionalized surface shear of 4.8. These values together with a mixed layer depth of 50 m were used to run the spec-

tral instability code used above. The results were then converted to dimensional units.

The presence of surface gravity waves plays an important role in determining whether or not the classical Ekman spiral is unstable. In the absence of surface gravity waves, the mean Ekman spiral is only slightly unstable to Langmuir cells (Fig. 12d). Maximum growth rates are about 10^{-4} s⁻¹, roughly the same size as the Coriolis frequency. The unstable cells also have very long (over 200 m) wavelengths. In the presence of surface gravity waves (Fig. 12c), the Ekman spiral is destabilized strongly. The fastest-growing mode is oriented about 15 deg to the right of the wind and has a wavelength of 25–30 m, much more in accord with the data. The growth rate of such a mode is 0.002 s⁻¹, implying a growth time of less than 10 minutes. This suggests that an Ekman spiral was not seen within the unstratified mixed layer during MILDEX, because it was unstable to Langmuir cells driven by wave–current interaction. In order to verify this hypothesis, it is necessary to estimate whether the finite-amplitude cells were capable of modifying the velocity profile. This is done in the following section.

7. Results from finite-difference code runs

This section demonstrates that large eddies driven by wave–current interaction were capable of modifying the velocity profile predicted by a MY2 model during MILDEX. It considers the results of a finite-difference code used to integrate Eqs. (13), (14) given the parameters in section 6. The angle of cell orientation was chosen to be 15 deg based the instability code run in section 6. The results are indicative of the potential importance of wave–current interaction in modifying the velocity profile. They do not constitute a full prediction of the velocity structure, since such a prediction would need to include some information on the time variability of wind, waves, and eddy viscosity and a better estimation of the effects of density (interaction with the thermocline and time-variable heat flux). Such effects are beyond the scope of this paper.

The velocity signals associated with the finite-amplitude cells are roughly the same size as those associated with the mean Ekman spiral. Figure 13 shows the streamfunction, alongcell velocity, and vertical velocity fields predicted by the finite-difference code at a time $t = 147$, corresponding roughly to one-dimensional day. After one day, the finite-difference code predicts a flow field dominated by cells with a wavelength of roughly 200 m. The cells are strongly asymmetric, with downwelling plumes of up to 0.06 m s⁻¹ and weaker upwelling zones where the vertical velocity is only about 0.02 m s⁻¹. The cells advect plumes of water moving quickly in the alongcell direction. The alongcell velocity associated with the plumes at mid-depth is 0.02–0.03 m s⁻¹ faster than the mean mixed layer velocity and 0.03–0.04 m s⁻¹ faster than the mean velocity in the mixed layer interior.

These finite-amplitude Langmuir cells replace small-scale diffusion as the principal mechanism by which the wind stress is distributed within the mixed layer. Figure 14 shows the velocity structure observed during MILDEX and various models. The observed and predicted shear structure is shown in Fig. 15. The velocity and shear profiles from the one-dimensional models are reproduced from Fig. 2. The profiles generated by the finite-difference code are averages over the last inertial

period, after the startup transients had died off and the eddy kinetic energy had stabilized.

The velocity structure in the presence of finite-amplitude Langmuir cells is very different from that in the absence of cells. The finite-difference code predicts a mixed layer in which there is a strongly sheared layer near the surface of the mixed layer, very little shear in the middle of the mixed layer, and more shear at greater depths. The structure of the velocity and shear profiles
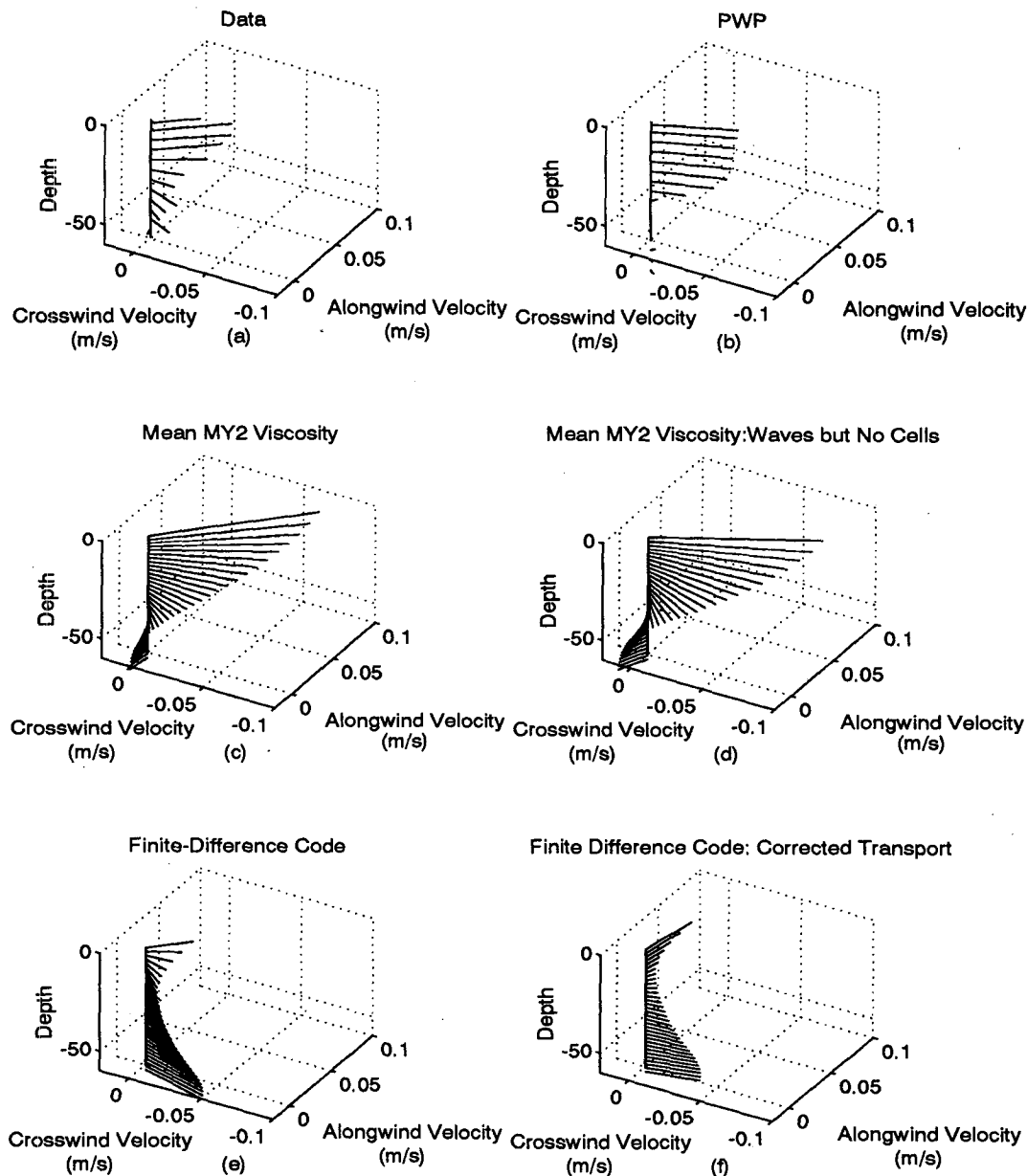
FIG. 14. Mean low-frequency velocity structure during MILDEX, 6–11 November. (a) Data. (b) Modeled by PWP model. (c) Modeled given mean eddy viscosity from MY2 model, but no waves. (d) Modeled given mean eddy viscosity from MY2 model, Pierson–Moskowitz spectrum, but without Langmuir cells. (e) Modeled using finite-difference code. (f) Velocity structure from finite-difference code corrected so as to give the same transport as the data.
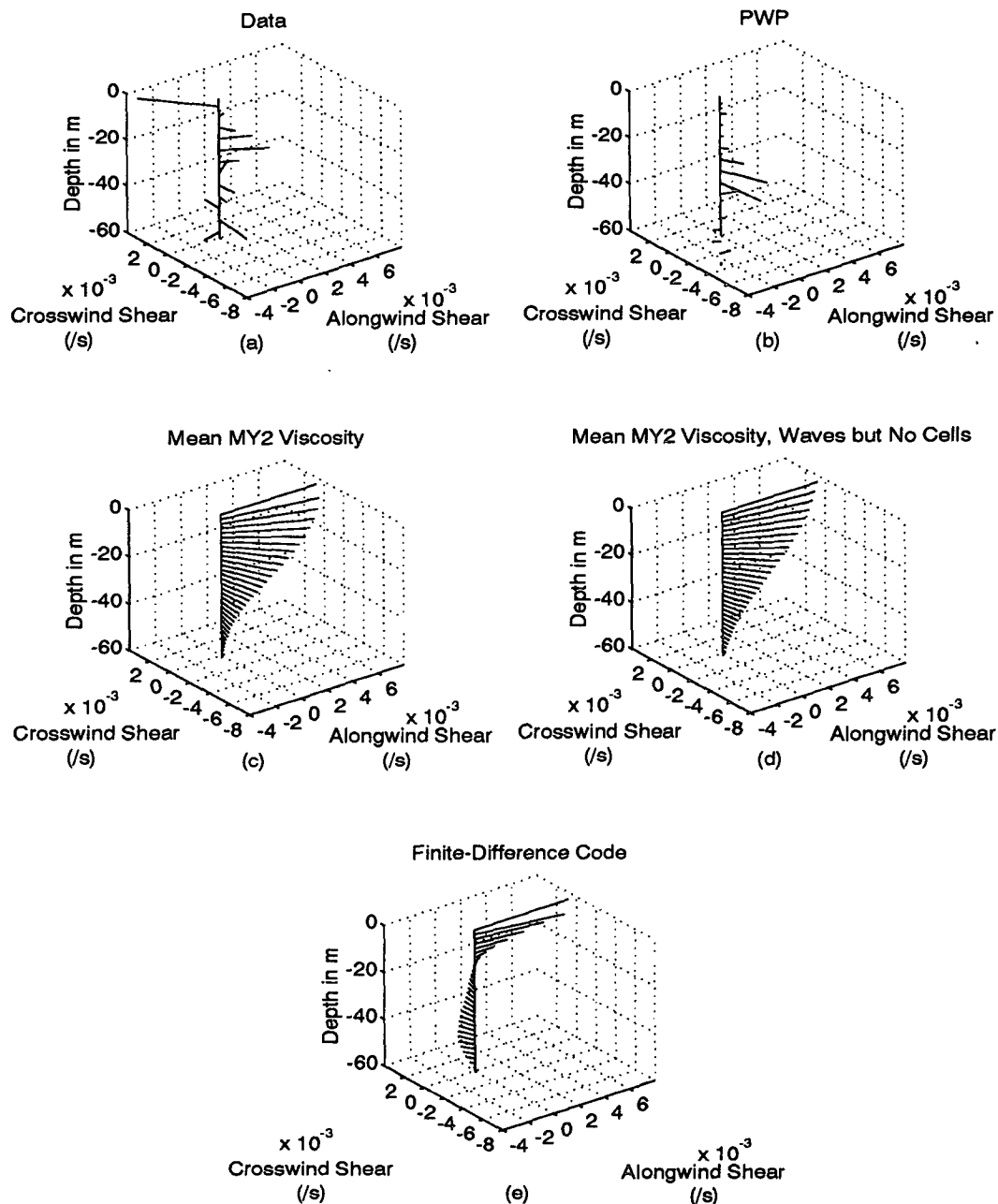
FIG. 15. Mean low-frequency shear structure during MILDEX, 6–11 November. (a) Data. Note the strong upwind shear near the surface. (b) Modeled by PWP model. (c) Modeled given mean eddy viscosity from MY2 model, but no waves. (d) Modeled given mean eddy viscosity from MY2 model, Pierson–Moskowitz spectrum, but without Langmuir cells. (e) Modeled using finite-difference code. Although the finite-difference code does get the magnitude of the observed shear right, it gets the direction wrong.

is very different from that predicted in the absence of Langmuir cells by the MY2 model. In general, the velocity profile is more uniform than predicted by the MY2 model. However, there are still shears within the mixed layer, a phenomenon seen in the data which contrasts sharply with the PWP model. The details of this shear structure, however, still differ significantly from

observations. Differences between the finite-difference code and the data (of which there are several) are considered in more detail in the following section.

In general, the finite-difference code seems to show more and deeper mixing than actually observed during MILDEX. This supports the hypothesis that Langmuir cells rather than small-scale turbulent motions are the

primary mechanism for stirring the mixed layer and that such cells need to be included in mixed layer models. However, the differences between the model output and observations are evidence that the actual physics is probably more complex than that included in the finite-difference code—so that there is no simple way to patch the one-dimensional models at present.

8. Conclusions

This work argues that the mixed layer is primarily maintained by large eddies driven by wave–current interaction. Models of the mixed layer that do not include these large eddies fail to capture the observed velocity structure. If one predicts the structure of the open-ocean Ekman spiral using eddy viscosities derived from assuming small-scale turbulent mixing, the resulting velocity profile is frequently strongly unstable to Langmuir cells driven by surface gravity waves. These Langmuir circulations mix over the depth of the layer and replace small-scale diffusion as the primary mechanism for vertical transport of momentum within the mixed layer interior. As a result, the interior of the mixed layer is less sheared than predicted by one-dimensional eddy viscosity models, which assume mixing to be driven by small-scale turbulence. However, near the upper boundary, these strongly mixing Langmuir cells are weaker, and a near-surface shear layer in which the mixing is driven by small-scale turbulence is predicted. This near-surface shear layer is not predicted by one-dimensional slab models (such as the PWP model), which assume complete and total homogenization of the mixed layer.

In the Northern Hemisphere, Langmuir cells that grow upon the Ekman spiral are oriented to the right of the wind, as observed in the field (Faller 1964). This orientation results from the cells responding to the rotation of the shear to the right of the wind. Presumably, observations in the Southern Hemisphere should show the cells as being oriented to the left of the wind. In both hemispheres, however, strong propagation of oceanic swell at some angle to the wind can result in the cells choosing a different angle of orientation, subject to the constraints outlined in section 5.

The numerical models of Langmuir circulation in the presence of Coriolis force presented here yield useful insights into the physics governing mixing in oceanic surface layers. However, there are still major differences between the theory as currently stated and observations of Langmuir cells. Three important discrepancies are listed below:

- The presence of waves was predicted to induce an Eulerian return flow balancing the Lagrangian transport associated with the Stokes drift. This return flow was not observed during MILDEX and has not been seen in other experiments (Price et al. 1987; Gnanadesikan 1994; Schudlich and Price 1994; Weller and Plueddemann 1995).[4]

- The shear in the near-surface shear layer was predicted to be downwind (with water near the surface moving more quickly in the alongwind direction than water slightly deeper in the water column). At greater depths, on the other hand, the finite-difference code predicts upwind shear. The reverse was seen at both depths during MILDEX.

- The horizontal length scale of the cells is extremely large (approximately 200 m), with no smaller scales present. Observations of the horizontal scale of the cells have often shown a range of scales (Weller and Price 1988; Zedel and Farmer 1991).

As noted in section 7, to some degree the failure of the finite-difference code to exactly reproduce the observed structure is attributable to the fact that the observations occurred in an environment where the forcing functions varied over time and the effects of density were not considered. However, certain inadequacies in the physics of the finite-difference code may also be important. The remainder of this section considers where the finite-difference code may be failing for intrinsic physical reasons and considers what might be done to improve the situation.

The failure of the model to reproduce the range of length scales and the near surface shear are potentially linked. Short-wavelength Langmuir cells act over shallower depths, growing more quickly than long-wavelength cells, but penetrate less deeply into the water column (Gnanadesikan 1994). Strong Langmuir cells near the surface could potentially produce a shear reversal similar to that caused by the long-wavelength cells. Such strong near-surface cells might also weaken the longer-wavelength cells, reducing the amount of momentum they are capable of transporting over the entire mixed layer and reducing the deep upwind shears.

The difference between the observed and predicted transport is more difficult to explain. One possible explanation for the difference is that the waves are represented by infinite length wave trains rather than by finite length groups. McIntyre (1981) points out that the mean volume flux associated with a wave group consists of three components:

1) That associated with the Stokes drift, which is trapped to the group itself.

2) A return flow that has a deeper structure but which is also trapped to the group.

---

[4] Fortunately, for MILDEX, the presence of an Eulerian return flow does not greatly alter the shear structure of the mixed layer (Fig. 15). As a result, it should not greatly change the instability characteristics of the mixed layer. This is not necessarily the case for smaller values of Ek.
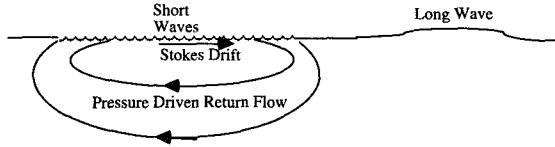
FIG. 16. Schematic of the mass fluxes associated with a finite-length wave group in deep water (after McIntyre 1981). The Stokes drift associated with the wave train contributes one component. However, the orbital velocities associated with the wave train are larger under the center of the wave train. This results in a surface depression trapped to the wave train, which drives a return flow. A third component, the long wave which balances the pressure depression, propagates away from the group at long gravity wave speeds. All three components have the same absolute value of mass transport.

3) A long wave that propagates away from the group.

A schematic of this is shown in Fig. 16. The magnitude of the volume transport associated with all three of these components is exactly equal. In the presence of the Coriolis force, all three components will exert a body force on the fluid. In the presence of mixing, however, the body forces associated with the wave group may cancel, while that associated with the long wave may contribute to the barotropic response of the entire water column.

In summary, Langmuir cells have the potential to play a major role in the physics of the oceanic surface layer. However, simple finite-difference code models do not yield accurate predictions of the mixed layer structure due to uncertainties in the physics of Langmuir cells as well as inadequacies in the model runs (lack of time dependence in particular). For more progress to be made, the following issues will need to be addressed:

• How to consistently specify the wave–Coriolis force interaction, given finite length wave groups and the correspondingly complicated structure of the mass transport.

• How to model turbulence and Langmuir cells in parallel so as to realistically model interactions with the thermocline.

• How to produce the range of scales seen in the ocean. The problem may lie in the parameterization of the mixing, the lack of three-dimensionality, or other as yet unspecified mechanisms.

APPENDIX

Models of the Mixed Layer Used in This Paper

a. One-dimensional mixed layer models

1) THE PRICE ET AL. (1986) SLAB MODEL

This model consists of two regions, a slab mixed layer and a transition layer directly underneath. Within the transition layer, adjacent boxes are mixed until the gradient Richardson number

$$\mathrm{Ri}_g = \frac{g \Delta\rho \Delta z}{\rho_0 \Delta U^2} = \frac{1}{4}. \tag{A1}$$

The mixed layer deepens as the result of two processes, buoyant overturning, which occurs whenever the water within the mixed layer is denser than the water immediately below it, and "bulk Kelvin–Helmholtz instability." This latter process occurs when the bulk Richardson number

$$\mathrm{Ri}_b = \frac{g \Delta\rho D}{\rho_0 \Delta U^2} = 0.65, \tag{A2}$$

where D is the mixed layer depth and $\Delta\rho$ and ΔU are defined across the base of the mixed layer. This term represents a parameterization of large eddies that homogenize the mixed layer rapidly.

2) MELLOR–YAMADA LEVEL-2 MODEL

In the Mellor–Yamada level-2 model, diffusion is parameterized with eddy diffusion coefficients K_m and K_ρ for momentum and density, respectively,

$$(K_m, K_\rho) = qL(S_m(\mathrm{Ri}), S_\rho(\mathrm{Ri})), \tag{A3}$$

where q is a typical turbulence velocity, L is a typical turbulence length scale, and S_m and S_ρ are functions of the local gradient Richardson number Ri_g. The turbulent velocity is set by the energy balance equation

$$\frac{q^3}{B_1 L} = K_m \left[\left(\frac{\partial U}{\partial z} \right)^2 + \left(\frac{\partial V}{\partial z} \right)^2 \right]$$
$$+ K_\rho \frac{g}{\rho} \left(\frac{\partial \rho}{\partial z} \right) \tag{A4}$$

dissipation = shear production + buoyancy transport,

where B_1 is a constant. Here L is set using the traditional Blackadar formulation

$$L = L_0 \frac{\kappa z}{\kappa z + L_0} \tag{A5a}$$

$$L_0 = 0.20 \int zq\,dz \Big/ \int q\,dz, \tag{A5b}$$

where κ is the Kolomogorov constant 0.4. For most neutrally stratified layers L_0 is of order 10 m, so that L is of order 5 m.

b. Two-dimensional models of instability

1) GALERKIN CODE

If the streamfunction, alongcell velocity, and Stokes drift are expanded as a Fourier series:

$$\psi = \Psi(z) + \psi(x, z, t) = \sum_{n=1}^{\infty} \Psi_n \sin\left(\frac{n\pi z}{D}\right)$$

$$+ \sum_{n=1}^{\infty} \psi_n(t) \sin\left(\frac{n\pi z}{D}\right) e^{ikx} \quad \text{(A6a)}$$

$$v = V(z) + v(x, z, t) = \sum_{n=1}^{\infty} V_n \cos\left(\frac{n\pi z}{D}\right)$$

$$+ \sum_{n=1}^{\infty} v_n(t) \sin\left(\frac{n\pi z}{D}\right) e^{ikx} \quad \text{(A6b)}$$

$$u_s = u_s(z) \sum_{n=1}^{\infty} u_{s_n} \cos\left(\frac{n\pi z}{D}\right) \quad \text{(A6c)}$$

$$v_s = v_s(z) = \sum_{n=1}^{\infty} v_{s_n} \cos\left(\frac{n\pi z}{D}\right). \quad \text{(A6d)}$$

In everything that follows, the horizontally varying series will be considered the perturbation. These series are truncated at some number N for the horizontally varying part (the second summation) and at $2N + 1$ for the horizontal mean part. A matrix equation for the ψ_n, v_n, ρ_n can then be defined:

$$\frac{\partial \psi_n}{\partial t} = \sum_{m=1}^{N} (U_{sp_{nm}} + P_{p_{nm}} + D_{p_{nm}})\psi_m$$

$$+ \sum_{m=0}^{N} (E_{v_{nm}} + V_{s_{nm}})v_m \quad \text{(A7a)}$$

$$\frac{\partial v_n}{\partial t} = \sum_{m=0}^{N} (U_{sv_{nm}} + P_{v_{nm}} + D_{v_{nm}})v_m$$

$$+ \sum_{m=1}^{N} (E_{p_{nm}} + V_{p_{nm}})\psi_m. \quad \text{(A7b)}$$

Here D_v and D_p represent viscous damping and are given by

$$D_{v_{nm}} = D_{p_{nm}} = -\text{La}\left(k^2 + \frac{n^2\pi^2}{D^2}\right)\delta_{nm}. \quad \text{(A8)}$$

The effects of Coriolis forces are given by E_v and E_p

$$E_{v_{nm}} = \frac{Fn\pi/D}{k^2 + n^2\pi^2/D^2}\delta_{nm} \quad \text{(A9a)}$$

$$E_{p_{nm}} = -F\frac{n\pi}{D}\delta_{nm}. \quad \text{(A9b)}$$

Left to themselves these matrices produce an inertial oscillation whose frequency asymptotes to a minimum of F at $k = 0$.

The advection of vorticity as the result of crosscell Eulerian flow and Stokes drifts is given by P_p and U_{sp}, respectively,

$$P_{p_{nm}} = \frac{-ik\pi/2D}{k^2 + n^2\pi^2/D^2}\left[|m - n|\left(k^2 + \frac{n^2\pi^2}{D^2}\right.\right.$$

$$\left.- \frac{|m - n|^2\pi^2}{D^2}\right)\Psi_{|m-n|} - (m + n)$$

$$\times \left(\frac{k^2 + n^2\pi^2}{D^2} - \frac{(m + n)^2\pi^2}{D^2}\right)\Psi_{m+n}\right] \quad \text{(A10a)}$$

$$U_{sp_{nm}} = -\frac{ik}{2}\frac{k^2 + \frac{m^2\pi^2}{D^2}}{k^2 + \frac{n^2\pi^2}{D^2}}(u_{s_{|n-m|}} - u_{s_{n+m}}). \quad \text{(A10b)}$$

The Craik–Leibovich vortex force is represented by V_s:

$$V_{s_{nm}} = \frac{ik\pi/2D}{k^2 + n^2\pi^2/D^2}((n - m)v_{s_{|n-m|}}$$

$$+ (n + m)v_{s_{n+m}}). \quad \text{(A11)}$$

Turning to the alongcell velocity advection terms, the cross-stream advection of perturbation velocity is represented by P_v:

$$P_{v_{nm}} = -\frac{ik\pi}{2D}(|n - m|\Psi_{|n-m|}$$

$$+ (n + m)\Psi_{n+m}) \quad n > 0 \quad \text{(A12a)}$$

$$P_{v_{0m}} = -\frac{ik\pi}{2D}m\Psi_m. \quad \text{(A12b)}$$

Similarly, the advection of mean alongcell velocity by the perturbation flow V_p is given by

$$V_{p_{nm}} = -\frac{ik\pi}{2D}(-(n - m)V_{|n-m|}$$

$$+ (n + m)V_{n+m}) \quad n > 0 \quad \text{(A13a)}$$

$$V_{p_{0m}} = -\frac{ik\pi}{2D}(-mV_m), \quad \text{(A13b)}$$

and the matrix representation of the advection of the alongcell velocity by cross-stream Stokes drift U_{sv} is

$$U_{sv_{nm}} = -\frac{ik}{2}(u_{s_{|n-m|}} + u_{s_{n+m}}) \quad n > 0 \quad \text{(A14a)}$$

$$U_{sv_{0m}} = -\frac{ik}{2}(mu_{s_m}). \quad \text{(A14b)}$$

The code was tested for a number of cases where F = 0, and the Stokes drift shear and Eulerian shear were constant with depth (similar to section 5). For N = 10, the error found was less than 1 part in 10^4. All runs in this work are for N = 40.

2) APPROXIMATE GALERKIN

In the Galerkin code of appendix section b(1) the effect of the Coriolis force on the unstable rolls arises from the E_p and E_v matrices in (A8a,b). If these matrices are set equal to zero, the instabilities do not feel the effect of Coriolis forces even though the mean flow upon which they are growing does. While this is not mathematically consistent, such a code can be used to estimate the importance of the Coriolis force in establishing the instability.

Similarly, all the terms involved with shear instability are in the shear/streamfunction interaction matrices P_p, U_{sp}, and D_p. The eigenvalues of $P_p + U_{sp} + D_p$ thus give the growth rates due to shear instability alone given the background Stokes drift and Eulerian shears.

c. Full two-dimensional model (finite-difference code)

This code uses a simple forward-difference time step, Arakawa Jacobians to evaluate the nonlinear advection terms, and simple centered differencing to evaluate the diffusion (Roache 1977). The grid used for the simulation in section 7 had 256 points in the horizontal and 32 in the vertical, modeling a dimensional space 400 m wide and 50 m deep. The code was initialized with perturbations at a variety of wavelengths (corresponding to 1, 2, 3, 4, 8, 12, and 16 cycles within the domain). The relatively naive handling of the diffusion and time stepping can lead to unrealistic numerical diffusion if the time step is too large. For the MILDEX case, the code was run for 32 000 time steps corresponding to approximately 1 pendulum day, so that each time step was approximately 3 s. For such a small time step the numerical diffusion was found to be insignificant when growth rates predicted from the code were compared to analytical solutions.

REFERENCES

Agarwal, Y. G., E. A. Terray, M. A. Donelan, P. A. Hwang, A. J. Williams, W. M. Drennan, K. K. Kahma, and S. A. Kitaigorodskii, 1992: Enhanced dissipation of kinetic energy beneath surface waves. *Nature*, **359**, 219–221.

Brown, R. A., 1970: A secondary flow model for the planetary boundary layer. *J. Atmos. Sci.*, **27**, 742–757.

Case, K. M., 1960: Stability of inviscid plane Couette flow. *Phys. Fluids*, **3**, 143–148.

Craik, A. D. D., and S. Leibovich, 1976: A rational model for Langmuir circulation. *J. Fluid Mech.*, **73**, 401–426.

Davis, R. E., R. DeSzoeke, and P. Niiler, 1981: Variability in the upper ocean during MILE. Part II: Modelling the mixed layer response. *Deep-Sea Res.*, **28**, 1427–1452.

Denman, K. L., 1973: A time-dependent model of the upper ocean. *J. Phys. Oceanogr.*, **3**, 173–185.

Ekman, V. W., 1905: On the influence of the earth's rotation on ocean currents. *Arkiv. Math. Astron. Phys.*, Vol. 2, No. 11.

Faller, A. J., 1964: The angle of windrows in the ocean. *Tellus*, **16**, 363–370.

Gammelsrød, T., 1975: Instability of Couette flow in a rotating fluid and the origin of Langmuir circulations. *J. Geophys. Res.*, **80**, 5069–5075.

Gottleib, D., and S. A. Orszag, 1977: *Numerical Analysis of Spectral Methods: Theory and Applications*. Soc. Ind. Appl. Math., 170 pp.

Gnanadesikan, A., 1994: Dynamics of Langmuir circulations in oceanic surface layers. Ph.D. dissertation. MIT/WHOI Joint Program in Physical Oceanography. WHOI Tech Rep. 94-23, 354 pp.

Hasselmann, K., 1970: Wave-driven inertial oscillations. *Geophys. Fluid Dyn.*, **1**, 463–502.

Huang, N. E., 1979: On the surface drift currents in the ocean. *J. Fluid Mech.*, **91**, 191–208.

Langmuir, I., 1938: Surface motion of water induced by wind. *Science*, **87**, 119–123.

Leibovich, S., 1983: The form and dynamics of Langmuir circulation. *Ann. Rev. Fluid Mech.*, **15**, 391–427.

Lele, S., 1985: Some problems of hydrodynamic stability arising in geophysical fluid dynamics. Ph.D. thesis, Cornell University, 302 pp.

McIntyre, M. E., 1981: On the "wave-momentum" myth. *J. Fluid Mech.*, **106**, 331–347.

Mellor, G., and T. Yamada, 1974: A hierarchy of turbulence closure models for planetary boundary layers. *J. Atmos. Sci.*, **31**, 1791–1806.

Mourad, P., 1995: Theoretical analysis of the initiation of Langmuir circulations in the ocean. *J. Phys. Oceanogr.*, submitted.

Pierson, W. J., and L. Moskowitz, 1964: A proposed spectral form for fully developed wind seas based on the similarity theory of S. A. Kitaigorodskii. *J. Geophys. Res.*, **69**, 5191–5203.

Price, J. F., R. A. Weller, and R. Pinkel, 1986: Diurnal cycling: Observations and models of the upper ocean response to diurnal heating, cooling and wind mixing. *J. Geophys. Res.*, **91**, 8411–8427.

Richman, J. G., R. A. deSzoeke, and R. E. Davis, 1987: Measurements of near-surface shear in the ocean. *J. Geophys. Res.*, **92**, 2851–2858.

Rieder, K. F., J. A. Smith, and R. A. Weller, 1994: Observed directional characteristics of the wind, wind stress, and surface waves on the open ocean. *J. Geophys. Res.*, **99**, 22 589–22 596.

Roache, P. J., 1977: *Computational Fluid Dynamics*. Hermosa, 434 pp.

Schudlich, R. R., and J. F. Price, 1994: The Ekman Spiral during the LOTUS 4 Experiment. *J. Phys. Oceanogr.*, submitted.

Weber, J. E., 1983: Steady wind and wave-induced currents in the open ocean. *J. Phys. Oceanogr.*, **13**, 524–530.

——, and A. Melsom, 1993: Volume flux induced by wind and waves in a saturated sea. *J. Geophys. Res.*, **98**, 4739–4745.

Weller, R. A., 1981: Observations of the velocity response to wind forcing in the upper ocean. *J. Geophys. Res.*, **86**, 1969–1977.

——, and J. F. Price, 1988: Langmuir circulations in the oceanic surface layer. *Deep-Sea Res.*, **35**, 711–747.

——, and A. J. Plueddemann, 1995: Observations of the mean vertical structure of the oceanic boundary layer. *J. Geophys. Res.*, submitted.

——, D. L. Rudnick, C. C. Eriksen, K. L. Polzin, N. S. Oakey, J. W. Toole, R. W. Schmitt, and R. T. Pollard, 1991: Forced ocean response during the Frontal Air–Sea Interaction Experiment. *J. Geophys. Res.*, **96**, 8611–8639.

Xu, Z., and A. J. Bowen, 1994: Wave- and wind-driven flow in water of finite depth. *J. Phys. Oceanogr.*, **24**, 1850–1866.

Zedel, L., and D. Farmer, 1991: Organized structures in subsurface bubble clouds: Langmuir circulation in the open ocean. *J. Geophys. Res.*, **96**, 8889–8900.